

# Merging Hierarchical Triple Black Hole Systems with Intermediate-mass Black Holes in Population III Star Clusters

Shuai Liu<sup>1,2</sup>, Long Wang<sup>2\*</sup>, Yi-Ming Hu<sup>2†</sup>, Ataru Tanikawa<sup>3</sup> and Alessandro A. Trani<sup>4,5,6</sup>

<sup>1</sup>Physics Department, School of Electronic and Electrical Engineering, Zhaoqing University, Zhaoqing 526061, People's Republic of China

<sup>2</sup>School of Physics and Astronomy, Sun Yat-sen University, Zhuhai 519082, People's Republic of China

<sup>3</sup>Department of Earth Science and Astronomy, College of Arts and Sciences, The University of Tokyo, 3-8-1 Komaba, Meguro-ku, Tokyo 153-8902, Japan

<sup>4</sup>Niels Bohr International Academy, Niels Bohr Institute, Blegdamsvej 17, 2100 Copenhagen, Denmark

<sup>5</sup>Research Center for the Early Universe, School of Science, The University of Tokyo, Tokyo 113-0033, Japan

<sup>6</sup>Okinawa Institute of Science and Technology, 1919-1 Tancha, Onna-son, Okinawa 904-0495, Japan

Accepted XXX. Received YYY; in original form ZZZ

## ABSTRACT

Theoretical predictions suggest that very massive stars have the potential to form through multiple collisions and eventually evolve into intermediate-mass black holes (IMBHs) within Population III star clusters that are embedded in mini dark matter haloes. In this study, we investigate the long-term evolution of Population III star clusters, including models with a primordial binary fraction of  $f_b = 0$  and 1, using the  $N$ -body simulation code `PETAR`. We comprehensively examine the phenomenon of hierarchical triple black holes in the clusters, specifically focusing on the merging of their inner binary black holes (BBHs), with post-Newtonian correction, by using the `TSUNAMI` code. Our findings suggest a high likelihood of the inner BBHs containing IMBHs with masses on the order of  $O(100)M_\odot$ , and as a result, their merger rate could be up to  $0.1\text{Gpc}^{-3}\text{yr}^{-3}$ . In the model with  $f_b = 0$ , the evolution of these merging inner BBHs is predominantly driven by their gravitational wave radiation at an early time, but their evolutionary dynamics are dominated by the interaction between them and tertiary BHs in the case with  $f_b = 1$ . The orbital eccentricities of some merging inner BBHs oscillate over time periodically, known as the Kozai-Lidov oscillation, due to dynamical perturbations. Furthermore, the merging inner BBHs tend to have highly eccentric orbits at low frequency range, some of them with low redshift would be detected by LISA/TianQin. In the higher frequency range, the merging inner BBHs across a wider redshift range would be detected by DECIGO/ET/CE/LIGO/KAGRA.

**Key words:** methods: numerical – galaxies: star clusters: general – stars: black holes – stars: Population III

## 1 INTRODUCTION

A class of black holes (BHs) with masses ranging from  $10^2 M_\odot$  to  $10^5 M_\odot$ , known as intermediate-mass black holes (IMBHs), is speculated to exist in the gap between stellar-mass black holes (SBHs) and massive black holes (MBHs) in the Universe. IMBHs have attracted significant attention due to their potential role in explaining the formation of MBHs in the first hundreds of millions of years after the Big Bang (Volonteri 2010; Wu et al. 2015; Bañados et al. 2018; Greene 2012; Reines & Comastri 2016; Mezcua 2017; Inayoshi et al. 2020; Greene et al. 2020; Wang et al. 2021b), as well as the anomalies observed in dwarf galaxies (DGs), e.g., core-cusp and the number of DGs (Silk 2017; Barai & de Gouveia Dal Pino 2019). In particular, IMBHs could serve as seeds for the formation of MBHs through their coalescence and gas accretion. Moreover, the early feedback from IMBHs could quench star formation (SF), reduce the number of DGs, and impact the central density profile of DGs.

Considerable efforts have been dedicated to the search for IMBHs so far, but concrete observations of them are scarce. Electromagnetic

wave (EM) observations have yielded some candidates, but they can not be identified as IMBHs conclusively. Ultraluminous x-ray sources as IMBH candidates in external galaxies and active galactic nuclei (AGN), e.g., M82 (Portegies Zwart et al. 2004), Galaxy ESO 243-49 HLX-1 (Farrell et al. 2012), NGC 2776 (Mezcua et al. 2015), could potentially be explained as SBHs with super-Eddington accretion. Globular clusters, including M15 (Gerssen et al. 2002, 2003; van der Marel et al. 2002) and G1 (Gebhardt et al. 2002, 2005), as well as  $\omega$ -Centauri (Baumgardt 2017; Noyola et al. 2008), are also considered possible locations for IMBHs, but the velocity dispersion of center stars caused by potential IMBHs could alternatively be explained by a concentrated group of SBHs or neutron stars, a stellar-mass binary black hole (SBBH), or radial anisotropy configuration (Hurley 2007; Zocchi et al. 2017; Baumgardt et al. 2019). Fortunately, the detection of gravitational waves (GWs) has brought a breakthrough in the search for IMBHs. The merger remnant of the SBBH called GW190521 (Abbott et al. 2020a) detected by LIGO/Virgo is a BH with a mass of  $\sim 142M_\odot$ , falling within the mass range of IMBHs. This marks the first direct observational evidence for the existence of IMBHs. Subsequently, several similar events, e.g., GW190426\_190642 (Abbott et al. 2021) has also been

\* E-mail: wanglong8@mail.sysu.edu.cn

† E-mail: huyiming@mail.sysu.edu.cn

detected. However, binary black holes (BBHs) consisting of IMBHs have not been detected directly by LIGO/Virgo/KAGRA yet. It has been suggested that the primary component of GW190521 may be an IMBH (Fishbach & Holz 2020; Nitz & Capano 2021), but this claim is still under debate. The challenge in the direct detection of IMBHs arises from the fact that the frequencies of GWs emitted by heavier BBHs with IMBHs are lower than the sensitive frequency bands of the current ground-based detectors. However, upcoming space-borne GW detectors, such as TianQin (Luo et al. 2016), Taiji (Ruan et al. 2020), LISA (Amaro-Seoane et al. 2017) and DECIGO (Kawamura et al. 2011), as well as the next generation ground-based GW detectors Cosmic Explorer (CE) (Reitze et al. 2019) and Einstein Telescope (ET) (Punturo et al. 2010), are expected to have sensitivities at lower frequency ranges, making them capable of detecting BBHs with IMBHs across a wide range of redshifts (Fregeau et al. 2006; Amaro-Seoane & Freitag 2006; Amaro-Seoane et al. 2007, 2009; Mapelli et al. 2010; Gair et al. 2011; Yagi 2012; Rasskazov et al. 2020; Jani et al. 2019; Emami & Loeb 2020; Arca Sedda & Mastrobuono-Battisti 2019; Datta et al. 2021; Arca-Sedda et al. 2021; Deme et al. 2020; Fragione et al. 2020; Liu et al. 2022; Wang et al. 2022; Fragione et al. 2022b; Garg et al. 2022; Fragione & Loeb 2023; Torres-Orjuela et al. 2023).

While searching for IMBHs, various possible explanations for their formation have been proposed, which could be divided into three categories roughly. The first one involves the mergers of stellar-mass objects in a dense environment. For example, successive or runaway mergers of SBHs in GCs could produce IMBHs with masses greater than  $10^3 M_{\odot}$  (e.g. Miller & Hamilton 2002; Gültekin et al. 2004; Giersz et al. 2015; Mapelli et al. 2021, 2022; Rizzuto et al. 2021; Mouri & Taniguchi 2002; Giersz et al. 2015). In environments with higher density, e.g., circumnuclear giant H II region (e.g. Taniguchi et al. 2000) and nuclear star clusters (e.g. Antonini et al. 2019; Fragione & Silk 2020; Kroupa et al. 2020; Fragione et al. 2022a; Rose et al. 2022), massive IMBHs would form, because the gravitational potential from galaxies could prevent merger remnants with natal kick from escaping from clusters, where the natal kick could be from supernovae (SNe) and dynamical few-body interactions, as well as recoil kick from asymmetric GW radiation. Secondly, IMBHs could form in gaseous environments. In AGN disks around MBHs, IMBHs could form through mergers of stars due to mass migration and subsequent gas accretion (McKernan et al. 2012, 2014). IMBHs may also be formed by the direct gravitational collapse of metal-poor giant gas without the formation of stars at the galactic centre (e.g. Mayer et al. 2010, 2015). Lastly, IMBHs could be formed through the evolution of very massive stars (VMSs) with low metallicities. In regions of starburst SF with high central densities, the successive mergers of massive stars could produce VMSs, which would then evolve to IMBHs (e.g. Portegies Zwart & McMillan 2002; Portegies Zwart et al. 2004, 2006; Freitag et al. 2006; Kremer et al. 2020; González et al. 2021), or even collapse to IMBHs directly without pair-instability SNe (Spera & Mapelli 2017).

Population III (PopIII) star clusters are also potential formation sites for VMSs which could evolve to IMBHs (Sakurai et al. 2017a). Most PopIII stars are massive, and they could merge to VMSs or become IMBHs, due to their extremely low metallicities (Stacy et al. 2016; Chon et al. 2021a; Latif et al. 2022). If PopIII clusters are embedded in mini dark matter haloes (e.g. Skinner & Wise 2020), the haloes would prevent them from being disrupted by the galactic potential, allowing them to survive from the early stage of the Universe to the present (Wang et al. 2022).

In prior investigations regarding the formation of IMBHs within PopIII star clusters, Sakurai et al. (2017a) delved into the formation

of VMSs within PopIII star clusters through the utilization of a zoom-in cosmological simulation. Furthermore, Reinoso et al. (2018) examined the impact of stellar collisions on the formation of VMSs by  $N$ -body simulations.

Wang et al. (2022) studied the long-term evolution of PopIII star clusters in mini dark matter haloes using the star-by-star  $N$ -body code `PETAR`, as well as the GW mergers of BBHs consisting of IMBHs. Several previous studies also investigated merging BBHs formed from isolated PopIII binaries (Belczynski et al. 2004, 2017; Kinguawa et al. 2014, 2020, 2021a,b,c; Hartwig et al. 2016; Inayoshi et al. 2017; Tanikawa et al. 2021a,b; Santoliquido et al. 2023; Costa et al. 2023) and PopIII star clusters (Liu & Bromm 2020a,b; Liu et al. 2021). Merging BBHs in triple systems formed dynamically in PopIII clusters are not explored, although many papers suggested BBHs formed from isolated or dynamical PopI/II triple/quadruple systems for GW sources (Antonini et al. 2014a; Silsbee & Tremaine 2017; Rodriguez & Antonini 2018; Fragione & Kocsis 2019; Hamers & Safarzadeh 2020; Trani et al. 2022).

In this study, we first examines triple systems comprising IMBH or BH components dynamically formed in PopIII clusters depending on the framework proposed by Wang et al. (2022). Nevertheless, it's important to acknowledge certain limitations in the models introduced by Wang et al. (2022). Firstly, these models do not incorporate primordial binaries. Although the characteristics of primordial binaries within PopIII clusters remain uncertain at present, observations of young clusters indicate a prevalence of multiple systems among OB stars (Sana et al. 2012; Duchêne & Kraus 2013; Gaia Collaboration et al. 2022), suggesting that this trend might extend to PopIII stars as well. Furthermore, in the models presented by Wang et al. (2022), binary mergers are handled using the orbital average method (Peters & Mathews 1963; Peters 1964). However, this method may not provide a robust description of their orbital evolution, especially when they exist within multiple systems (Antonini et al. 2014b).

In this investigation, we conduct additional simulations, adhering to the initial conditions outlined in (Wang et al. 2022), to enhance the statistical robustness of our results. Simultaneously, we undertake a series of simulations that incorporate primordial binaries. Furthermore, for triple BHs with merging inner BBHs (hereinafter referred to simply as “merging triple BHs”) formed in the `PETAR` simulation, we evolve their orbits using the direct few-body numerical code including post-Newtonian (PN) correction `TSUNAMI`, and study GWs from their merging inner BBHs under perturbation.

The rest of this paper is organized as follows: we present the initial conditions of PopIII clusters, and the  $N$ -body and few-body methods (codes) in Sec. 2. The population properties of merging triple BHs and GWs emitted by their inner BBHs are investigated in Sec. 3. Finally, we draw the conclusion in Sec. 4. Throughout the paper, geometrical units ( $G = c = 1$ ) are used, unless otherwise specified, and the standard  $\Lambda$ CDM cosmological model (Ade et al. 2016) is adopted.

## 2 METHOD

The complete process to track the long-term evolution of PopIII clusters and to evolve merging triple BHs within them is depicted in Fig. 1, where a schematic diagram of merging triple BHs is illustrated in Fig. 2. It can be divided into two main parts: simulations of PopIII clusters using an integrated approach combining the  $N$ -body code `PETAR` with single and binary population synthesis code `BSEEMP`, as well as simulations of merging triple BHs using the high-accuracy method with the PN correction `TSUNAMI` based on the results obtained

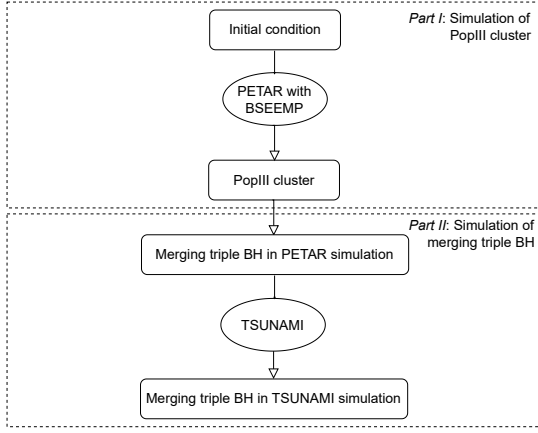


**Figure 1.** The flow chart outlines the complete process of evolving merging triple BHs in PopIII clusters, which consists of two main parts: simulations of PopIII clusters and simulations of merging triple BHs, respectively. Rectangles and ellipses represent target physical systems and methods (codes), respectively.

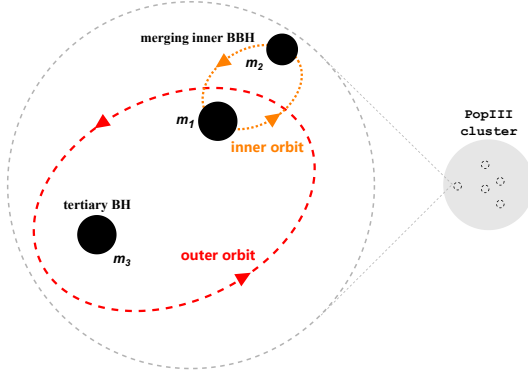


**Figure 2.** A sketch of merging triple BHs in PopIII clusters. The gray ball represents a PopIII cluster, in which small gray dashed circles are merging triple BHs. The enlarged version of a merging triple BH is in a gray large dashed circle, where a merging inner BBH with primary mass  $m_1$  and secondary mass  $m_2$  ( $m_2 \leq m_1$ ) orbits around a tertiary BH with mass  $m_3$ . Orange dotted and red dashed circles are inner orbit with semimajor axis  $a_1$  and outer orbit with semimajor axis  $a_2$ , respectively.

from the cluster simulations. These two parts will be explained in the following two subsections in detail, respectively.

## 2.1 Simulation of PopIII cluster

### 2.1.1 PETAR

We simulate the evolution of PopIII clusters using the high-performance  $N$ -body code PETAR (Wang et al. 2020b), which combines the particle-tree and particle-particle (P<sup>3</sup>T) algorithm (Oshino et al. 2011) with the slow-down algorithmic regularization (SDAR) method (Wang et al. 2020a). The P<sup>3</sup>T component of the code handles long-range gravitational interactions and is implemented within the framework of PENTACLE (Iwasawa et al. 2017) and the Framework for Developing Particle Simulator (Iwasawa et al. 2016; Iwasawa et al. 2020). Conversely, the SDAR method is employed to manage short-range interactions, ensuring precise and efficient treatment of binary orbital evolution and close encounters. Additionally, the impact of

the galactic potential on PopIII clusters is implemented by Galpy (Bovy 2015).

### 2.1.2 BSEEMP

The single and binary stellar evolution in PopIII clusters is simulated by the fast population synthesis method BSEEMP (Tanikawa et al. 2020), which could trace the stellar wind mass loss and BH formation of PopIII stars with the minimum metallicity  $Z = 2 \times 10^{-10}$ . The details of star evolution in BSEEMP and the definition of production of star evolution are explained in (Hurley et al. 2000, 2002; Tanikawa et al. 2020, 2021b; Wang et al. 2022). For instance, the BHs within pair-instability mass gap, ranging from  $60M_{\odot}$  to  $121M_{\odot}$ , are referred to as “pair-instability BHs” (PIBHs). The BHs with mass greater than  $121M_{\odot}$  and less than  $60M_{\odot}$  are known as IMBHs and low-mass BHs (LBHs), respectively.

### 2.1.3 Initial condition

The initial conditions for the PopIII clusters in this study are derived from the long-term model “NFWden\_long\_w9\_noms\_imf1” introduced in (Wang et al. 2022). We select this model as it is expected to lead to the formation of VMSs, which eventually evolve to IMBHs with the mass up to  $10^3M_{\odot}$ . In order to improve statistical accuracy, we carry on 10 times more simulations, each using different random seeds. Additionally, we include a new set of models that incorporate the presence of primordial binaries. The specific key parameters of these models are highlighted as follows.

The initial mass of clusters  $M_{\text{clu}}$  is set to  $10^5M_{\odot}$ , similar to that of Model A, which is one of star clusters embedded in mini-haloes models in (Sakurai et al. 2017b). The initial half-mass radius  $r_h = 1\text{pc}$  is a typical value observed in star clusters. The central density model for clusters in (Michie 1963; King 1966) is adopted, where the central concentration is determined by the ratio between the core radius  $r_c$  and the tidal radius  $r_t$  of clusters, denoted as  $W$ . The initial value of  $W$  is set to  $W_0 = 9$ .

The initial mass function (IMF) of stars in PopIII clusters is anticipated to follow a single power-law profile with a index of approximately -1 based on the hydrodynamic simulations (Stacy et al. 2016; Chon et al. 2021b; Latif et al. 2022)

$$p(m) \propto m^{-\alpha}, m_{\min} < m < m_{\max}, \quad (1)$$

where  $m_{\min}$  and  $m_{\max}$  are the upper and lower limits of the IMF respectively. Compared to the canonical IMF with the power index of -2.35 (e.g., Kroupa 2001; Chabrier 2003), the IMF of PopIII star clusters would be top-heavy, favoring more massive stars. This condition is expected to result in more BHs. Therefore, we simply set the power index  $\alpha = -1$  to represent this heavy tail and assume the upper and lower limits of the IMF to be classical values, i.e.,  $m_{\min} = 1M_{\odot}$  and  $m_{\max} = 150M_{\odot}$ .

As the structure of the dark matter halo where the PopIII clusters embed is unclear to date, its potential is assumed to follow the model in (Navarro et al. 1996),

$$\Phi = -\frac{M_{\text{vir}}}{r[\log(1+C(z)) - C(z)/(1+C(z))]\log(1+r/r_{\text{vir}})}, \quad (2)$$

where the virial mass  $M_{\text{vir}} = 4 \times 10^7M_{\odot}$ , the virial radius  $r_{\text{vir}} = 280\text{pc}$  and the concentration follows  $C(z) = C(0)/(1+z)$ , with the assumption that clusters evolve from  $z = 20$  to the present, and  $C(0) = 15.3$ .

The properties of primordial binaries in PopIII clusters are still uncertain, and the observations of the young SF region show that

OB stars are mostly in binaries or high-order multiple systems (Sana et al. 2012; Duchêne & Kraus 2013; Gaia Collaboration et al. 2022), which could be applicable to PopIII clusters as well. In this study, we introduce a set of models featuring similar initial conditions but with a primordial binary fraction of  $f_b = 1$ , with the characteristics of these binaries aligning with observational constraints derived from (Sana et al. 2012).

We employ `PETAR` and to evolve 168 PopIII clusters with  $f_b = 0$  and 1 for up to 12Gyr, respectively.

## 2.2 Simulation of merging triple BHs

### 2.2.1 `TSUNAMI`

Binary mergers in `PETAR` is handled by the orbital average method described in (Peters & Mathews 1963; Peters 1964), which may formally break down if the binary is orbited by the third object on a highly inclined orbit at a moderate distance (Antonini et al. 2014b). Therefore, we use `TSUNAMI` to evolve orbits of merging triple BHs in the `PETAR` simulation. `TSUNAMI` is a direct few-body numerical code (Trani et al. 2019; Trani & Spera 2022) used to evolve the dynamics of triple systems with high accuracy. It implements the Mikkola’s algorithmic regularization with a chain structure (Mikkola & Tanikawa 1999a,b), including 1PN and 2PN precession and 2.5PN GW radiation, as well as tidal interactions for stars and planets.

### 2.2.2 initial condition

The orbital evolution of merging triple BHs formed in PopIII clusters can be traced by `PETAR`. The parameters (masses, positions and velocities) of the components of merging triple BHs are recorded by `PETAR` at various of times between the first record and closing to merger times within the integrator time-step where inner BBHs are merging. The closing to merger time represents the moment when one component of an inner binary has a Schwarzschild radius larger than its Roche-lobe radius defined in (Eggleton 1983). We regard the parameters of merging triple BHs at the first record and closing to merger times in the `PETAR` simulation as the initial condition of `TSUNAMI` simulation, respectively.

Due to the dense star environment of PopIII clusters, merging triple BHs might be perturbed through encounters with field objects on timescales shorter than their evolution time, which would alter their orbital properties significantly or even disrupt them. The timescale for collision with field objects is (Binney & Tremaine 1987)

$$T_{\text{coll}} = 2 \times 10^5 \text{yr} \left( \frac{10^6 \text{pc}^{-3}}{n} \right) \left( \frac{\text{AU}}{a_2} \right) \left( \frac{30 M_\odot}{m_1 + m_2 + m_3} \right), \quad (3)$$

where  $n$  is the number density of PopIII clusters. The collision time is estimated up to be 10 Myr, depending on the average number density of PopIII clusters ( $\langle n \rangle = 100 \text{pc}^{-3}$  (Wang et al. 2022)), the average semimajor axis of outer binaries of merging triple BHs ( $\langle a_2 \rangle = 100 \text{AU}$ ) and the average total mass of them ( $\langle m_1 + m_2 + m_3 \rangle = 100 M_\odot$ ) in the `PETAR` simulations<sup>1</sup>.

We evolve merging triple BHs at the first record and closing to merger times in the `PETAR` simulation with `TSUNAMI` for up to 10 Myr respectively, and only keep the triple BHs whose inner BBHs could merge eventually, i.e., merging triple BHs in the `TSUNAMI` simulation.

<sup>1</sup> We select all the merging triple BHs in the `PETAR` simulation and make statistic on their semimajor axes and masses.

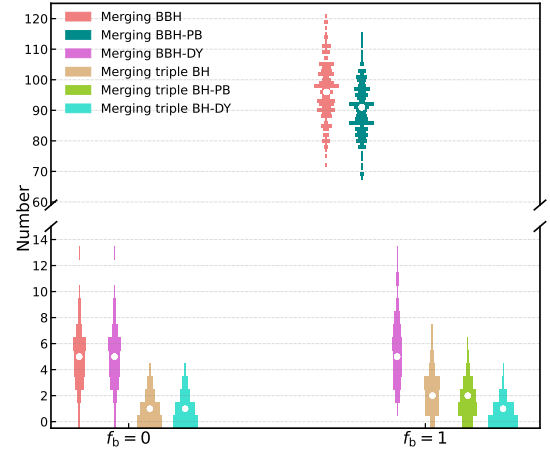


**Figure 3.** The number of merging triple BHs and merging BBHs during the evolution of PopIII clusters simulated by `PETAR`, which is denoted by box charts. A rectangle represents an integer, and its horizontal length denotes the probability distribution of the corresponding integer. The lightcoral color represents the total merging BBHs, of which ones formed by the evolution of primordial binaries and dynamical captures are denoted by suffixes “-PB” and “-DY”, respectively. The burlywood color represents the total merging triple BHs, the symbols representing the formation channels of their inner BBHs the same as those of merging BBHs. The white dots denote median values. The x-axis represents the cases with  $f_b$  of 0 and 1, respectively. Note that, in order to better presentation of the charts, the scales located above and below the truncation of the y-axis are set to be different.

## 3 RESULT

In this section, we investigate population properties of merging triple BHs and GWs emitted by their inner BBHs within PopIII clusters, along with the impact from  $f_b$  on them.

### 3.1 Number of merging triple BHs in `PETAR` simulation

We investigate the number of merging triple BHs and merging BBHs in the `PETAR` simulation, as shown in Fig. 3. In clusters without primordial binaries ( $f_b = 0$ ), all the merging BBHs naturally form through dynamical processes. On average, there are 5 merging BBHs in one cluster, with approximately one fifth of them occurring in merging triple BHs. If all the stars are paired initially, i.e.,  $f_b = 1$ , the average number of merging BBHs increases to  $\sim 100$ , with majority formed through the evolution of primordial binaries, and  $\sim 6\%$  formed by dynamical captures. The average number of the merging triple BHs also increase to 2, with most of them having inner BBHs originating from primordial binaries and a few formed through dynamical captures.

### 3.2 Comparison between merging triple BHs in `PETAR` and `TSUNAMI` simulation

In this subsection, we will compare merging triple BHs in the `PETAR` and `TSUNAMI` simulations. In order to express convenience hereinafter, we refer the merging triple BHs in the `PETAR` simulation to “`PETAR` merging triple BHs”. The merging triple BHs whose inner BBHs could evolve from the first record and closing to merger times of `PETAR` records to merge in the `TSUNAMI` simulation are referred to “`TSUNAMI` merging triple BHs (the first record time)” and “`TSUNAMI` merging triple BHs (closing to merger time)”, respectively.

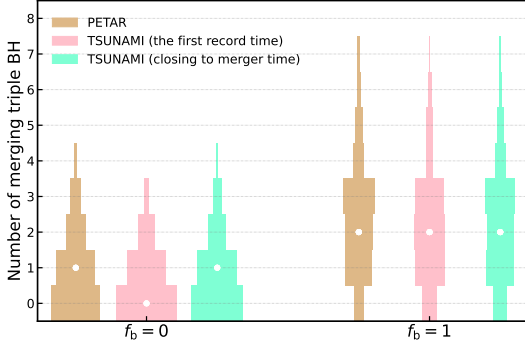


**Figure 4.** Comparison of the number of PETAR merging triple BHs and merging triple BHs in the TSUNAMI simulation. A rectangular box represents an integer, and its horizontal length denotes the probability distribution of the corresponding integer. The purple color represent PETAR merging triple BHs. The green and orange colors denote TSUNAMI merging triple BHs (the first record time) and TSUNAMI merging triple BHs (closing to merger time), respectively. The white dots denote median values. The x-axis represents cases with different values of  $f_b$ .

Fig. 4 provide a comparison among the numbers of the PETAR merging triple BHs ( $N_{\text{tbh,p}}$ ), the TSUNAMI merging triple BHs (the first record time;  $N_{\text{tbh,t0}}$ ), and the TSUNAMI merging triple BHs (closing to merger time;  $N_{\text{tbh,tf}}$ ). For models with  $f_b = 0$  and 1, we find that  $N_{\text{tbh,t0}} \lesssim N_{\text{tbh,tf}} \lesssim N_{\text{tbh,p}}$ . This will be explained in detail as follows.

The merging triple BHs selected for the initial conditions of the TSUNAMI simulations are those that have been ascertained to undergo mergers in the PETAR simulations. Consequently, if the TSUNAMI results exhibit a divergent orbital evolution for these triples, there exists the possibility that some of them may not culminate in mergers. When TSUNAMI adopts the initial conditions of merging triple BHs nearing the merger time from PETAR records, the inner BBHs are already in the advanced stages of merging. Consequently, this results lead to  $N_{\text{tbh,tf}}$  being greater than  $N_{\text{tbh,t0}}$  and comparable to  $N_{\text{tbh,p}}$ .

In the following, we will further study the difference between the PETAR merging triple BHs and TSUNAMI merging triple BHs (the first record time) providing more evolution information. Hereinafter, we only analyze TSUNAMI merging triple BHs (the first record time) and they are simply referred to “TSUNAMI merging triple BHs”.

We investigate evolution results of PETAR merging triple BHs in the TSUNAMI simulation, as listed in Table 1, and investigate their dynamical stability, which could lead to the difference between the PETAR and TSUNAMI simulations. In particular, stable triple systems have a constant semimajor axis of inner binaries on a secular timescale, unstable triple systems, in contrast, would experience chaotic energy exchange, leading to that one body escapes from the systems over a short timescale. The stability could be determined by the following criterion (Mardling & Aarseth 2001)

$$\frac{a_2}{a_1} > \frac{3.3}{1 - e_2} \left[ \frac{2}{3} \left( 1 + \frac{m_2}{m_1 + m_2} \right) \frac{1 + e_2}{(1 - e_2)^{1/2}} \right]^{2/5} \times (1 - 0.3i_{\text{mut}}/\pi), \quad (4)$$

where  $i_{\text{mut}}$  is the angle between inner and outer orbital planes. In the PETAR simulation, more than 50% merging triple BHs are stable in both cases with  $f_b = 0$  and 1. In the TSUNAMI simulation, almost all the stable PETAR merging triple BHs could also merge. However, more than half of unstable PETAR merging triple BHs have different evolution results (merge, break, and neither merge nor break) in the TSUNAMI simulation. This is an inevitable consequence of the chaotic

nature of triple systems. Small differences in the initial conditions or in the integration algorithm are bound to create differences in the evolution (Hayashi et al. 2022; Portegies Zwart et al. 2023). This is especially true for meta-stable or unstable triples, where the extreme chaotic behavior can amplify small differences of two neighboring solutions, until their macroscopic outcomes diverge (Lalande & Trani 2022; Portegies Zwart et al. 2022; Trani et al. 2024). Fortunately, it has been shown that, despite different final outcomes for an individual simulation can arise from small differences in accuracy, algorithms, or machine architectures, the statistical outcome of many realizations is independent from these factors (Suto 1991; Boekholt et al. 2020).

We compare orbital evolutions of several representative events in both PETAR and TSUNAMI simulations. Two stable merging triple BHs are shown in Fig. 5. In the first example (a), there are no discernible perturbations from the tertiary BHs. In the second example (b), significant perturbations from the tertiary BHs affect both the inner and outer BBHs. These two examples illustrate scenarios where either GW radiation or dynamical perturbations predominantly influence the orbital evolution of the inner binaries. To illustrate this distinction, we can employ an analytical criterion proposed by (Antonini et al. 2014b):

$$\ell_1 = \ell_{\text{GW}}, \quad (5)$$

where  $\ell_1 = \sqrt{1 - e_1}$  and  $\ell_{\text{GW}}$  are the defined dimensionless angular momenta of the inner BBHs and the critical angular momentum below which GW energy loss dominates its evolution, respectively.

For the example (a),  $\ell_1 < \ell_{\text{GW}}$ , the inner BBH decouples from the third BH and evolves as an isolated binary approximately. The orbital evolutions using these two codes consistently agree with each other, implying that the GW effects from the orbital averaged method in PETAR and the direct numerical integration including the PN correction method in TSUNAMI are practically identical for (almost) isolated binaries.

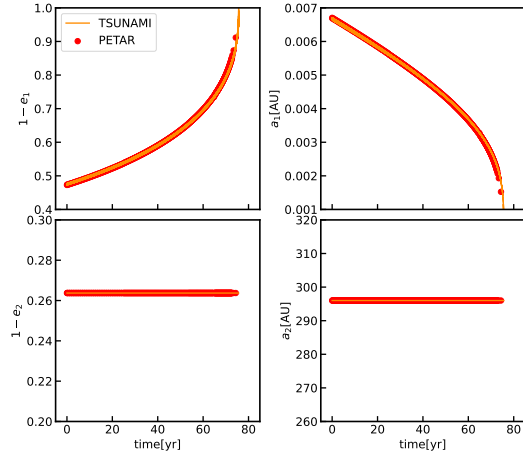
However, in the case of example (b), where  $\ell_1 > \ell_{\text{GW}}$ , while the orbital evolution using both codes appears similar in the early stages, they exhibit significant differences as time progresses. These differences between the results suggest that when the dynamical influence from the third BHs on the inner BBHs cannot be ignored, the numerical three-body integration including the PN correction method and the orbital-averaged method may not agree with each other anymore, which is consistent with the conclusion from (Antonini et al. 2014b).

An unstable triple BH whose inner BBH could merge in the PETAR simulation but break in the TSUNAMI simulation is also shown in Fig. 6. In the early stage of evolution, the evolutions in the PETAR and TSUNAMI simulations are nearly identical. However, with the evolution, the differences between these two simulations become more and more significant. In particular, at about 50 yr, the inner BBH starts to merge in the PETAR simulation. In contrast, the inner BBH gradually escapes from the gravitational influence of the third BH and the outer BH breaks apart eventually in the TSUNAMI simulation. This divergence in outcomes is a result of the difference between the two methods and the instability of triple BHs.

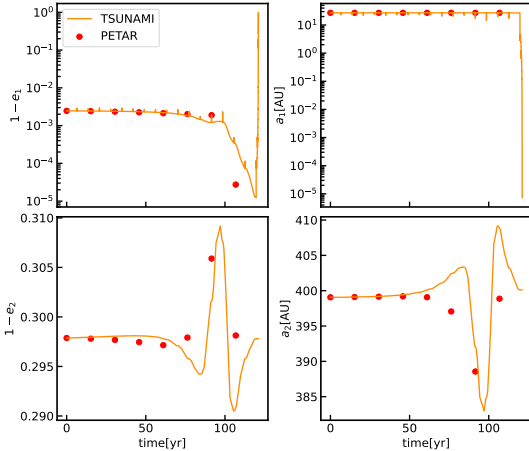
Triple systems may have interesting Kozai-Lidov (KL) oscillation, i.e.,  $e_1$  and  $i_{\text{mut}}$  oscillate quasi-periodically with time (Kozai 1962; Lidov 1962; Naoz 2016). The orbital evolution of several merging triple BHs with KL oscillation in the TSUNAMI simulation, along with them in the PETAR simulation, is shown in Fig. 7. The orbital elements, including  $e_1$  and  $i_{\text{mut}}$  are almost the same at early stage of evolution in both PETAR and TSUNAMI simulations. However, as the merging triple BHs evolve,  $e_1$  increases rapidly, leading to the merger of the inner BBHs within a short time in the PETAR simulation (note that the KL oscillation could also occur in the PETAR simulation, but

**Table 1.** Evolution results of PETAR merging triple BHs in the TSUNAMI simulation and their stabilities.

Code	$f_b$	Merge (stable)	Merge (unstable)	Break (stable)	Break (unstable)	Neither merge nor break (stable)	Neither merge nor break (unstable)
PETAR	0	101 (60.5%)	66 (39.5%)	–	–	–	–
	1	346 (84.6%)	63 (15.4%)	–	–	–	–
TSUNAMI	0	99 (59.3%)	19 (11.4%)	1 (0.6%)	47 (28.1%)	1 (0.6%)	0 (0.0%)
	1	339 (82.9%)	26 (6.4%)	1 (0.2%)	36 (8.8%)	6 (1.5%)	1 (0.2%)



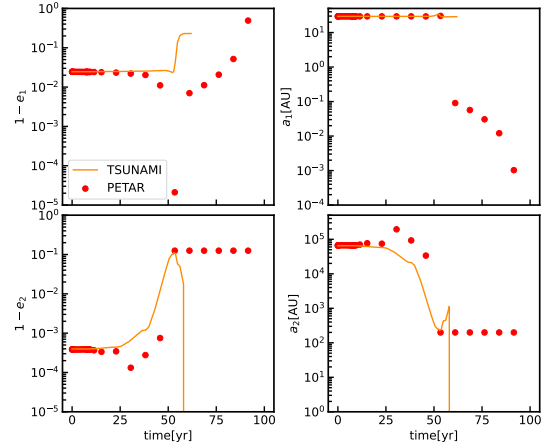
(a)



(b)

**Figure 5.** The evolution of orbital parameters of (a) one stable merging triple BH with  $m_1 = 200.1M_\odot$ ,  $m_2 = 53.3M_\odot$ ,  $m_3 = 44.8M_\odot$  and (b) one stable merging triple BH with  $m_1 = 350.6M_\odot$ ,  $m_2 = 49.2M_\odot$ ,  $m_3 = 55.6M_\odot$  in both PETAR and TSUNAMI simulations. The results from PETAR and TSUNAMI simulations are plotted in red dot and orange solid line, respectively. The x-axes are shifted by the time recorded.

due to the quick merger of the inner BBH and low time resolution, it is challenging to observe). On the other hand, in the TSUNAMI simulation, the merging triple BH exhibits quasi-periodic oscillations of  $e_1$  and  $i_{\text{mut}}$  over a very long period. For example, the last merging triple BH in the plot evolves about  $7 \times 10^4$  years in total, with a period of oscillation for  $e_1$  being  $\sim 7000$  years, which is consistent with the KL timescale analytically obtained by (Antognini 2015; Trani et al.

**Figure 6.** The evolution of orbital eccentricity (upper panel) and semimajor axis (lower panel) of an unstable triple BH with  $(m_1 = 56.1M_\odot, m_2 = 55.8M_\odot, m_3 = 33.7M_\odot)$  that the inner BBHs could merge in the PETAR simulation but break apart in the TSUNAMI simulation. The results from PETAR and TSUNAMI are plotted in red dot and orange solid line, respectively. The x-axes are shifted by the time recorded.

2022)

$$T_{\text{KL}} = P_1 \frac{m_1 + m_2}{m_3} \left( \frac{a_2}{a_1} \right)^3 (1 - e_2^2)^{3/2}, \quad (6)$$

where  $P_1 = 2\pi\sqrt{a_1^3/(m_1 + m_2)}$  is the Kepler period of the inner BBHs. Furthermore, we explore the effect of turning off the PN correction in the TSUNAMI simulation and observe the orbital evolution of these events. While  $e_1$  and  $i_{\text{mut}}$  undergo quasi-periodical oscillations, their behavior is distinct. Specially, at certain parameter regions,  $e_1$  in the TSUNAMI simulation without PN correction can be either smaller or larger than those in the TSUNAMI simulation, which consists of the prediction that the PN effect can suppress or excite  $e_1$  (Naoz et al. 2013).

Based on the above comparison, TSUNAMI (direct three-body numerical integration including the PN correction) provides a more realistic evolution of merging triple BHs. Therefore, in the following analysis, we focus on TSUNAMI merging triple BHs, unless explicitly stated otherwise.

### 3.3 Population property of merging triple BH

We investigate the mass distribution of merging triple BHs and compare it with that of merging isolated BBHs, as shown in Fig. 8. In the case of  $f_b = 0$ , both merging inner BBHs and merging isolated BBHs have primary masses  $m_1$  of  $\mathcal{O}(100)M_\odot$ , which are indicative of IMBHs. Their inner and isolated BBHs tend to be uncomparable, i.e., the mass ratio  $q_1 = m_2/m_1$  concentrates around 0.1. In contrast, in clusters with primordial binaries ( $f_b = 1$ ), the primary

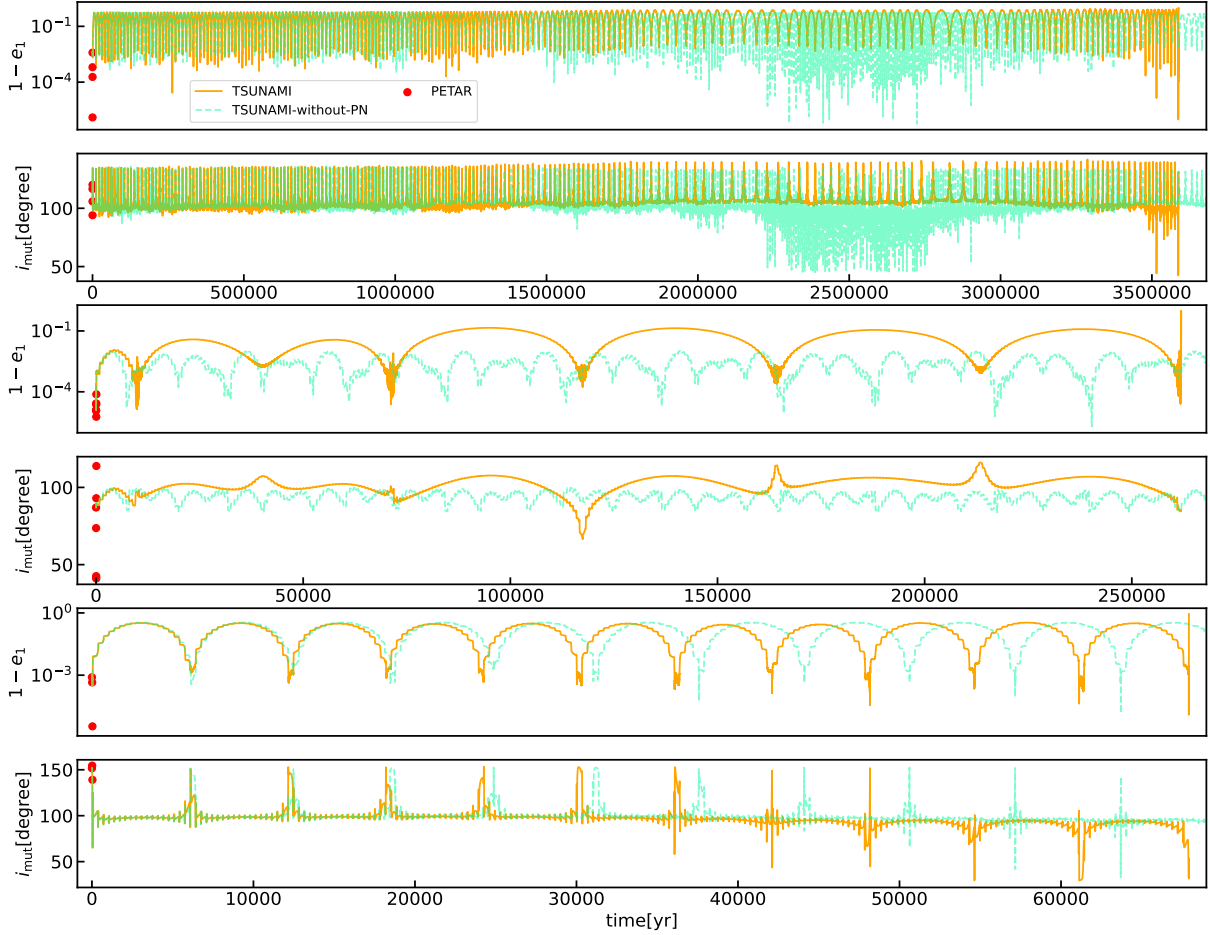


**Figure 7.** The orbital parameter evolutions ( $e_1$  and  $i_{\text{mut}}$ ) of three merging triple BHs with the KL oscillation, having the component masses of  $(m_1, m_2, m_3) = (50.58M_\odot, 41.97M_\odot, 33.44M_\odot)$ ,  $(153.19M_\odot, 432.74M_\odot, 53.60M_\odot)$ ,  $(56.35M_\odot, 101.98M_\odot, 53.60M_\odot)$  in the TSUNAMI simulation, are shown from the upper to lower panels, respectively. Each pair of adjacent panels corresponds to one event. The results in the PETAR and TSUNAMI simulations are plotted in red scatter and orange solid line, respectively. Additionally, the result in the TSUNAMI simulation without the PN correction is plotted in a gray dashed line (due to the lack of PN correction, the evolution time becomes much longer. For the convenience of comparison, a part of the evolution is truncated). The x-axes are shifted based on the time recorded.

masses  $m_1$  are typically  $O(10)M_\odot$ , and component masses tend to be comparable. We can understand the difference as follows.

In the model with  $f_b = 0$ ,  $r_b$  and  $r_c$  are smaller, as shown in Fig. 9, due to the absence of binary heating (Wang et al. 2021a). This lead to an environment with higher number density of objects. Therefore, compared to the case with  $f_b = 1$ , the formation of VMSs heavier than  $400M_\odot$  via multiple collisions, which can evolve to heavier BHs (Wang et al. 2022), becomes easier in the case with  $f_b = 0$ . In clusters with primordial binaries, most merging inner BBHs and merging isolated BBHs originate from primordial binaries, as shown in Fig. 3, which are expected to evolve into lighter BHs. In addition, BHs formed from the evolution of primordial binaries inherit the property of comparable mass, which results in a higher occurrence of mass ratios close to 1.

The mass distribution of merging BBHs inferred by LVKC based on GWTC-3 is also presented<sup>2</sup>. Compared to merging inner BBHs and merging isolated BBHs in PopIII clusters, they appear to be much lighter, which could be attributed to the observation selection effect of LIGO/Virgo. Since LIGO/Virgo are more sensitive at high

frequency band (hundreds of hertz), only merging comparable light BBHs with low redshifts are expected to be observed. Therefore, merging BBHs inferred by LVKC are biased towards lower masses. Regarding the outer BBHs of merging triple BHs, most of tertiary BHs  $m_3$  are  $O(10)M_\odot$  in both cases with  $f_b = 0$  and 1. However, the outer BBHs prefer to be comparable in the case with  $f_b = 1$ , because primordial binaries with comparable masses dominate the formation of merging triple BHs as well.

The distribution of orbital eccentricity and semimajor axis of merging triple BHs and merging isolated BBHs is shown in Fig. 11. In both of cases with  $f_b = 0$  and 1, due to the interaction with the tertiary BHs, merging inner BBHs tend to have significantly higher eccentricities. In contrast, merging isolated BBHs tend to have circular orbits as they lack the perturbation from the third BHs. Furthermore, since all the merging isolated BBHs are formed through dynamical captures in the case with  $f_b = 0$ , they are more eccentric than those formed from the evolution of primordial binaries, which inherently tend to have small eccentricities, in the case with  $f_b = 1$ . In both cases with  $f_b = 0$  and 1, the outer BBHs of merging triple BHs prefer to have large eccentricities ( $\sim 0.9$ ), due to the gravitational capture process between the inner BBHs and the third BHs. The

<sup>2</sup> The data is from <https://zenodo.org/record/7843926>

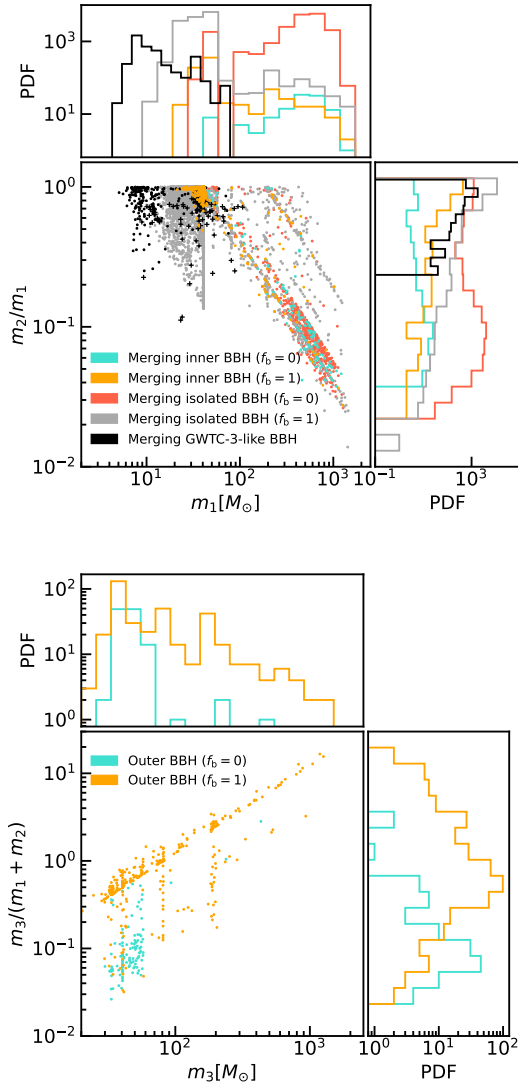


**Figure 8.** Upper: the distribution of the primary mass  $m_1$  and mass ratio  $m_2/m_1$ . Bottom: the distribution of the tertiary mass  $m_3$  and mass ratio  $m_3/(m_1 + m_2)$ . The symbol PDF means probability density function. The blue and orange colors denote merging triple BHs in the cases with  $f_b = 0$  and 1, respectively. In the corresponding cases, merging isolated BBHs are represented by red and gray colors, respectively. The black color denotes merging BBHs inferred by LVKC based on GWTC-3.

semimajor axes of the outer orbits tend to be much larger than those of the inner orbits, otherwise the latter would be disrupted by the tidal interaction. In addition, most merging triple BHs have large  $i_{\text{mut}}$  ranging from  $45^\circ$  to  $135^\circ$ , as shown in Fig. 12.

We also study the evolutionary dominance of inner BBHs of merging triple BHs at their first record time, as listed in Table 2. In the case with  $f_b = 0$ , the orbital evolution of more than 50% inner BBHs are dominated by the GW driven, while the evolutionary dominance is the dynamical interaction between them and the tertiary BHs in the case with  $f_b = 1$ . This discrepancy can be explained as follows. The inner BBH in the case with  $f_b = 0$  are more eccentric than those in the case with  $f_b = 1$ , as shown in Fig. 11. This makes that  $\ell_1$  is more likely to be smaller than  $\ell_{\text{GW}}$  in the case with  $f_b = 0$ .

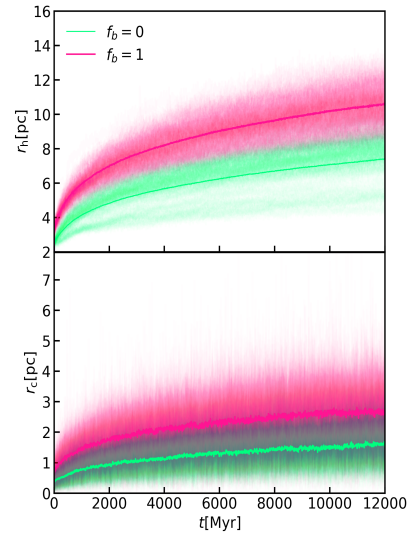


**Figure 9.** Upper: The evolution of  $r_h$  of PopIII clusters. Lower: The evolution of  $r_c$  of PopIII clusters. The cases with  $f_b = 0$  and 1 are plotted in springgreen and deeppink, respectively. The light colors represent 168 simulations, while the deep colors are mean values of them.

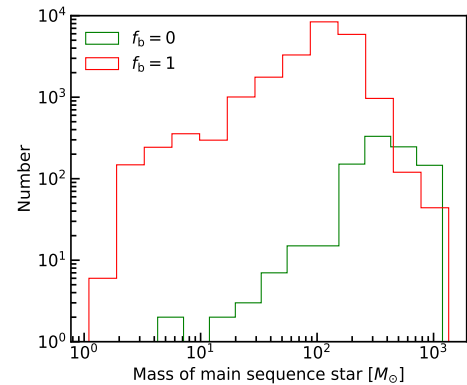


**Figure 10.** Mass distribution of main sequence stars from binary mergers. The y-axis represents the number of formed main sequence stars. The cases with  $f_b = 0$  and 1 are plotted in green and red colors.

**Table 2.** The evolutionary dominance of inner BBHs of merging triple BHs at the first record time.

$f_b$	Dynamical interaction ( $\ell_1 > \ell_{\text{GW}}$ )	GW driven ( $\ell_1 < \ell_{\text{GW}}$ )
0	22.0%	78.0%
1	61.6%	38.4%

### 3.4 Merger rate of inner BH-IMBH of merging triple BH

The merger remnants and merger times of inner BBHs of merging triple BHs are shown in Fig. 13. In both cases of  $f_b = 0$  and 1, the inner BBHs begin to merge at about 10Myr. The total number of mergers increases logarithmically with time approximately, following the standard distribution of merger time  $\propto t^{-1}$  (e.g. Tremou et al. 2018) until the present Universe, with about 80% occurring before 3000Myr ( $z > 2$ ). However, the values of  $f_b$  affect the mass spectrum of merger remnants significantly. Specifically, when  $f_b = 0$ , most remnants would be IMBHs with  $O(100)M_\odot$ . As  $f_b$  increases to 1,



**Table 3.** Average numbers and corresponding merger rates of inner BBHs of merging triple BHs and merging isolated BBHs over redshift per 12 Gyr in cases with  $f_b = 0$  and 1. These values are represented by  $n(\mathcal{R}_{\text{lower}} - \mathcal{R}_{\text{upper}})$ , where  $n$  represents the average number,  $\mathcal{R}_{\text{lower}}$  and  $\mathcal{R}_{\text{upper}}$  in the unit of  $\text{Gpc}^{-3}\text{yr}^{-1}$  are lower and upper limits of the average merger rate, respectively. The symbol BBH represents all the merging inner or merging isolated BBH, where IMBH-BH means binaries containing at least one IMBH, IMBBH denotes binaries composing of two IMBH, PIBH-LBH represents binaries consisting of PIBH and LBH, LBBH denotes binaries including two LBH. Some numbers are inconsistent due to rounding.

Type	$f_b$	BBH	IMBH-BH	IMBBH	PIBH-LBH	LBBH
Merging inner	0	0.7 (0.02-0.1)	0.6 (0.02-0.1)	0.03 (0.001-0.01)	0.03 (0.001-0.01)	0.05 (0.001-0.01)
	1	2.2 (0.1-0.4)	0.4 (0.01-0.1)	0.1 (0.003-0.02)	0.1 (0.002-0.02)	1.6 (0.04-0.3)
Merging isolated	0	3.9 (0.1-0.7)	3.4 (0.1-0.6)	0.2 (0.004-0.03)	0.1 (0.003-0.02)	0.4 (0.002-0.01)
	1	93.6 (2.5-15.6)	2.7 (0.1-0.5)	0.9 (0.03-0.2)	0.6 (0.02-0.1)	90.2 (2.4-15.0)

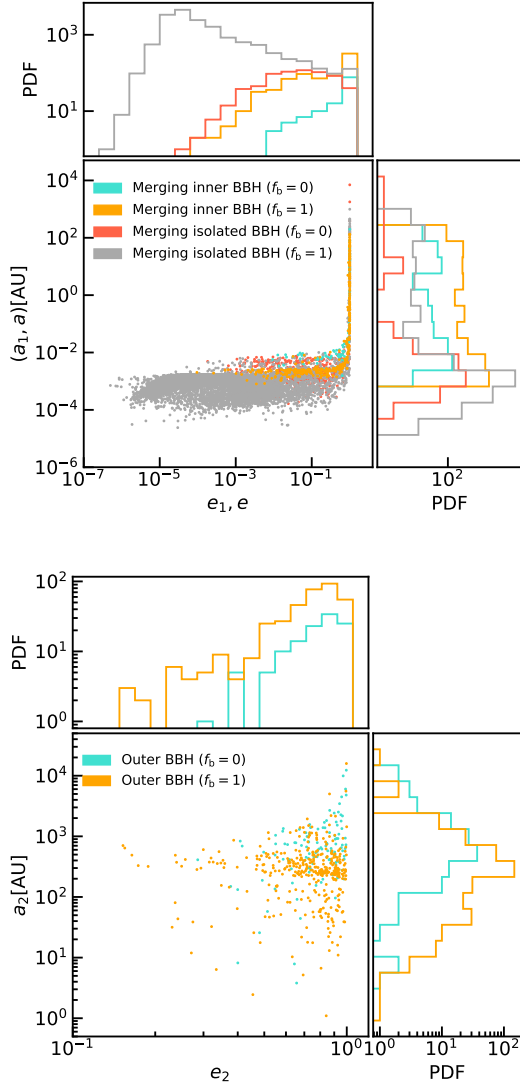


**Figure 11.** The distribution of orbital elements at the first record time. Upper: the distribution of the orbital eccentricity  $e_1$  ( $e$ ) and the semimajor axis  $a_1$  ( $a$ ) of the merging inner (isolated) BBHs. Bottom: the distribution of the orbital eccentricity  $e_2$  and the semimajor axis  $a_2$  of the outer BBHs of merging triple. The blue and orange colors denote the merging triple BHs in the cases with  $f_b = 0$  and 1, respectively. In the corresponding cases, the merging isolated BBHs are represented by red and gray colors, respectively.

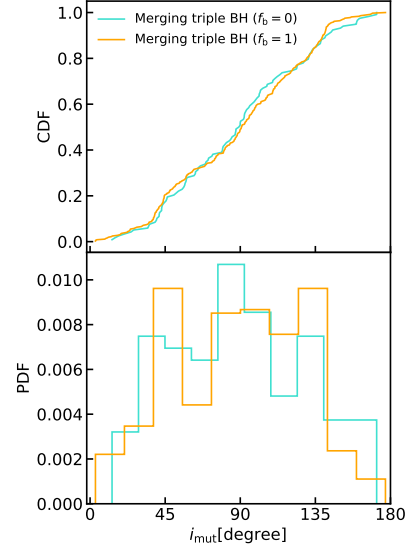


**Figure 12.** The distribution of angles  $i_{\text{mut}}$  between the inner and outer planes of merging triple BHs at the first record time. The upper and lower panels display the cumulative distribution function (CDF) and distribution of  $i_{\text{mut}}$ . The blue and orange colors correspond to the cases with  $f_b = 0$  and 1, respectively.

the remnants become lighter, with most of them being  $\mathcal{O}(10)M_\odot$ . We can understand the difference depending on Fig. 8 and the explanation on it.

For comparison, the merging isolated BBHs in cases with  $f_b = 0$  and 1 are also investigated. Their mergers follow the trend of inner BBHs of merging triple BHs roughly, but the number of them increases relatively slowly during the period of 200-5000Myr. This is because the isolated BBHs, without perturbation from other BHs, take more time to undergo mergers. For the influence of  $f_b$  on the remnant masses of merging isolated BBHs, it exhibits a similar trend to that of merging inner BBHs.

The merging inner and merging isolated BBHs can be categorized based on their component masses. The average number  $n$  of such mergers and their corresponding merger rates  $\mathcal{R}$  averaged over redshift are listed in Table 3, where  $\mathcal{R}$  can be estimated as below

$$\mathcal{R} = \frac{n}{M_{\text{clu}}/\text{SFR} \times T_{\text{evo}}} \quad (7)$$

where  $M_{\text{clu}} = 10^5 M_\odot$  and SFR are the total stellar mass and star formation rate of Pop III clusters, respectively. The lower and upper limits of the average SFR are  $3.2 \times 10^4 M_\odot \text{Mpc}^{-3}$  and  $2 \times 10^5 M_\odot \text{Mpc}^{-3}$  (Tanikawa et al. 2022; Skinner & Wise 2020; Inayoshi et al. 2021), respectively. In the case with  $f_b = 0$ , the merger rate of inner BBH

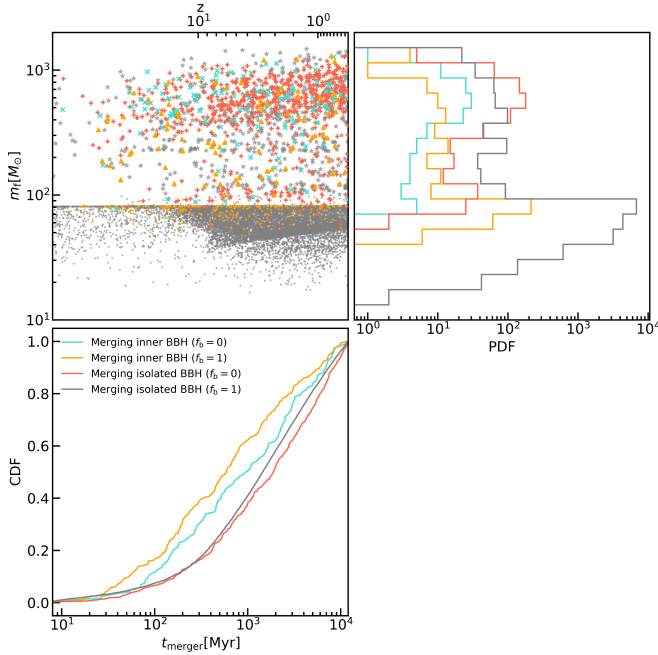


**Figure 13.** Upper: the merger remnant masses ( $m_f$ ) of inner BBHs of merging triple BHs and merging isolated BBHs in the cases with  $f_b = 0$  and 1, which are plotted in different colors and shapes, respectively. The merging inner BBHs and merging isolated BBHs from primordial binaries are marked with dots. Lower: the CDF of merger times ( $t_{\text{merger}}$ ) of inner and isolated BBHs in the cases with different values of  $f_b$ . The upper x-axis denotes the redshift  $z$  corresponding to  $t_{\text{merger}}$ .

reaches up to  $0.1\text{Gpc}^{-3}\text{yr}^{-1}$ , which are slightly larger than that of inner IMBH-BH. The upper merger rates of inner IMBBH, inner PIBH-LBH and inner LBBH are  $0.01\text{Gpc}^{-3}\text{yr}^{-1}$ . As  $f_b$  increases to 1, the merger rates increase by several to dozens of times, as expected, except for that of inner IMBH-BH. The slight decline in the merger rate of inner IMBH-BH could be attributed to the fact that most inner BBHs consist of comparable components with dozens of solar masses in the case with  $f_b = 1$ , as shown on the upper panel in Fig. 8. For merging isolated BBHs with different components, the upper merger rates are several to dozens of times those of corresponding inner BBHs in the case with the same  $f_b$ . Depending on these above results, the merger rate of inner and isolated IMBBH could make a contribution to that of IMBBH constrained by LIGO/Virgo/KAGRA collaboration (LVKC) (Abbott et al. 2022, 2019). If we regard PIBH-LBH and LBBH as GW190521-like sources and stellar-mass binary BHs (SBBHs) respectively, their merger rates could contribute to or explain those inferred by LVKC (Abbott et al. 2020a; Abbott et al. 2020b; Abbott et al. 2023).

### 3.5 GW from inner IMBH-BH of merging triple BH

Merging eccentric BBHs are accompanied by the emission of GWs consisting of different order harmonics, whereas only the second one is included in the case of circular orbits. The characteristic amplitude of the  $n$  order ( $n$ th) harmonic of inspiral GWs is given, following (Kremer et al. 2019), by

$$h_{cn} = \sqrt{\frac{2}{3\pi^4/3}} \frac{M^{5/6}}{D} f_n^{-1/6} \left(\frac{2}{n}\right)^{1/3} \sqrt{\frac{g(n, e)}{F(e)}}, \quad (8)$$

where  $f_n$  is the frequency of the  $n$ th harmonic,  $M$  and  $D$  are the chirp mass and distance of the merging BBHs, respectively. Among the harmonics, the ( $n_{\text{peak}} = f_{\text{peak}}/f_{\text{orb}}$ )th order one focused in the following has the maximum radiation power, where  $f_{\text{orb}}$  is the orbital frequency calculated by the Kepler's third law. The peak frequency  $f_{\text{peak}}$  can be obtained by (Hamers 2021)

$$f_{\text{peak}} = \frac{\sqrt{m_1 + m_2}}{\pi} \times \frac{1 - 1.01678e + 5.57372e^2 - 4.9271e^3 + 1.68506e^4}{[a(1 - e^2)]^{1.5}}, \quad (9)$$

where  $a$  and  $e$  are the semimajor axes and orbital eccentricities of merging BBHs, respectively. As the merging BBHs evolve in their orbits, they undergo successive stages of merger and ringdown after the inspiral stages, rendering Eq. (8) unsuitable. Due to the circularization of GW radiation, the orbital eccentricities of BBHs decrease and approach zero as they enter the merger and ringdown phases, making the ( $n_{\text{peak}} = 2$ )th harmonic become dominant. The GWs from the merger and ringdown phases could be described by PhenomD waveform (Husa et al. 2016; Khan et al. 2016). Considering the significant effect of cosmic expansion on the motion of distant merging BBHs, some physical quantities should be replaced with their redshifted counterparts:  $D \rightarrow D_L$  (luminosity distance),  $M \rightarrow (1+z)M$ ,  $f_n \rightarrow f_n/(1+z)$ , in both Eq. (8) and PhenomD waveform. Furthermore, the inspiral phase of merging BBHs can last much longer than the observation time of GW detectors, thus the fraction of mission lifetime sources spends within given frequency bins should be considered. Therefore, when calculating the characteristic strain of inspiral GWs, it should be multiplied by the square root of  $\min[1, \dot{f}_n(T_{\text{obs}}/f_n)]$  (D'Orazio & Samsing 2018; Willms et al. 2007; Sesana et al. 2005), where  $T_{\text{obs}} = 5$  years is adopted as a fiducial value here.

We calculate the  $f_{\text{peak}}$  and corresponding GWs from inner BBHs of merging triple BHs, and compare them with those from merging isolated BBHs depending on Eq. (8) and PhenomD waveform model. It should be noted that since calculating the orbital eccentricities and semimajor axes of merging inner BBHs with TSUNAMI will be not accurate anymore, when they begin to enter the bands of ground-based GW detectors like LIGO, because in this regime the PN approximation stops holding. Thus, we stop calculating them once  $a$  reaches  $O(10^{-4})\text{AU}$ . At this stage, GW radiation starts to dominate the evolution of merging inner BBHs and the perturbation from the tertiary BHs can be neglected safely, so we continue evolving the orbital of merging inner BBHs until  $a$  approaches zero alternatively by the averaged orbital Eqs. (10), which describes the evolution of merging isolated BBHs (Peters & Mathews 1963; Peters 1964)

$$\frac{da}{dt} = -\beta \frac{F(e)}{a^3}, \quad (10a)$$

$$\frac{de}{dt} = -\beta \frac{19}{12} \frac{e}{a^4(1-e)^{5/2}} \left(1 + \frac{121}{304} e^2\right). \quad (10b)$$

As for the merging isolated BBHs, since they are not perturbed throughout their whole evolution, we evolve them with Eqs. (10) until  $a$  approaches to zero.

The evolution of  $e_1$  with  $f_{\text{peak}}$  of all the inner BBHs, including inner IMBH-BH, within merging triple BHs, along with the corresponding characteristic strain of GWs emitted from them are shown in Fig. 14. In the cases with both  $f_b = 0$  and 1,  $e_1$  of some sources

<sup>3</sup> The power spectrum density of LIGO A+ is from <https://dcc.ligo.org/LIGO-T1800042/public>

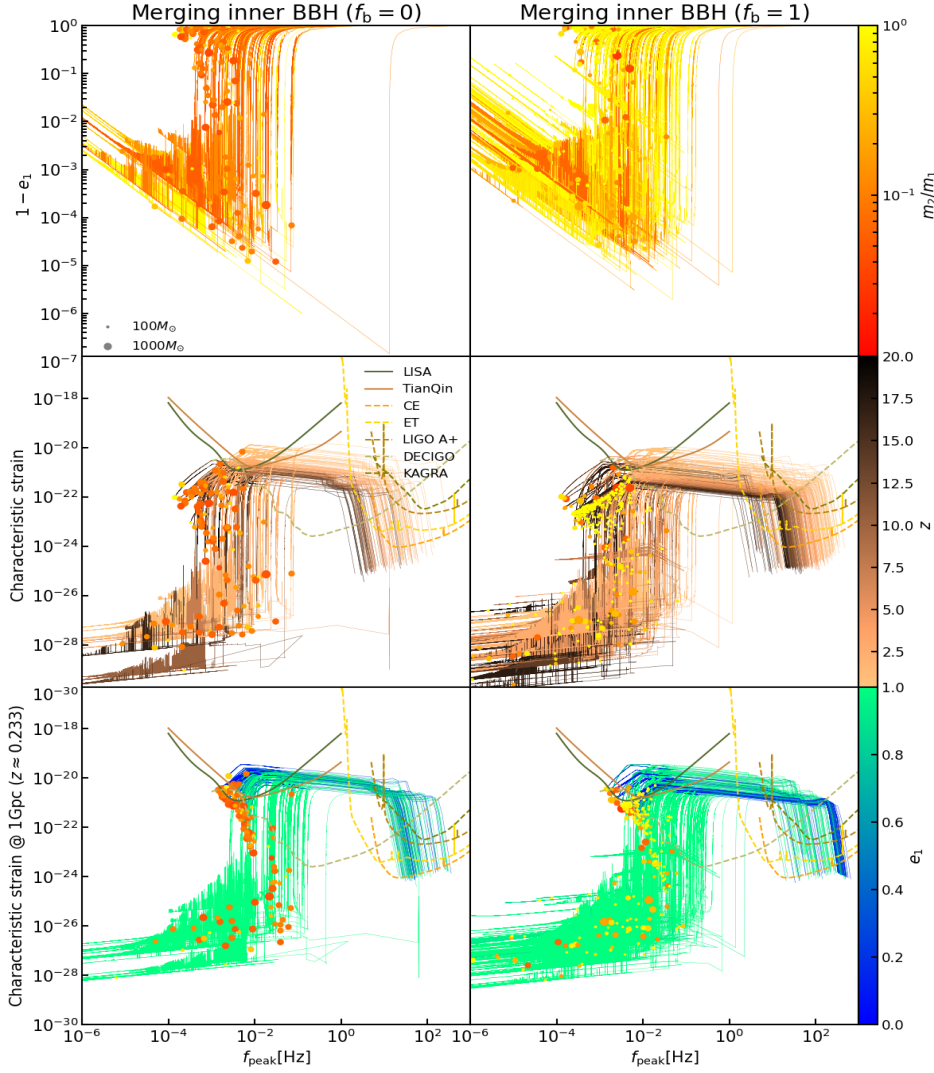


**Figure 14.** Inner BBHs of merging triple BHs. *Upper:* the evolution of inner orbital eccentricity  $e_1$  with  $f_{\text{peak}}$ , and the color bar denotes the inner mass ratio  $m_2/m_1$ . *Middle:* the characteristic strains of GWs with  $f_{\text{peak}}$ , and the color bar represents the redshift of sources. *Lower:* the characteristic strains of GWs from sources assumed to be at 1Gpc ( $z \approx 0.233$ ) with  $f_{\text{peak}}$ , and the color bar denotes the values of  $e_1$  at the first record time. The size of dots scales with the total mass of the merging inner BBHs, the characteristic strains of noise of GW detectors<sup>3</sup> (Kawamura et al. 2011; Robson et al. 2019; Wang et al. 2019; Michimura et al. 2020; Abbott et al. 2017; Hild et al. 2011) are plotted in different colors. The columns from left to right are cases with  $f_b = 0$  and 1, respectively.

always decreases, similar to those shown on the upper panel in Fig. 10 in (Wang et al. 2022)<sup>4</sup>. This occurs because these sources decoupled from the third BHs, as seen in the example (a) in Fig. 5, and their orbital evolution is dominated by GW radiation. However, the evolution of  $e_1$  of the remaining sources display peaks, oscillations and sharp turning points at lower frequencies before they evolve as isolated binary systems approximately. This is attributed to the oscillations of their orbital elements caused by the dynamical interactions between them and the third BHs before their GW radiation becomes dominant, as observed in the example (b) in Fig. 5 and other sources in Fig. 7. Most merging inner BBHs have detectable orbital eccentricities at LISA/TianQin bands. The distribution of  $e_1$

at  $f_{\text{peak}} = 0.01\text{Hz}$ <sup>5</sup> where LISA/TianQin is most sensitive is plotted on the upper panel in Fig. 16. Most of  $e_1$  are  $\mathcal{O}(0.01)$ , and a fraction of sources have  $e_1$  between 0.1 and 1. When the merging BBHs are at  $\sim 10\text{Hz}$  where CE/ET/LIGO/KAGRA become sensitive, they can be regarded as quasicircular due to the circularization of GW radiation, with  $e_1$  concentrating at  $10^{-4}$ , as shown on the lower panel in Fig. 16.

In both cases with  $f_b = 0$  and 1, the characteristic strains of GWs emitted by the merging inner BBHs decoupled from the third BHs are similar to those on the medium panel in Fig. 10 in (Wang et al. 2022)<sup>6</sup>. For the merging inner BBHs that are affected by the tertiary

<sup>4</sup> In fig. 10, when calculating the trajectory of  $a$  and  $e$  to depict the evolution of  $e$  and GW strains with peak frequency for all merging BBHs using Eqs. (10), it is assumed that the merging BBHs remain unaffected by perturbations from other objects.

<sup>5</sup> For the evolution of  $e_1$  which can reach around 0.01Hz multiple times through oscillation, we select the value of  $e_1$  corresponding to the last time.

<sup>6</sup> Fig. 10 in (Wang et al. 2022) did not account for the ringdown effect in calculating strains. Consequently, our results provide a more accurate representation of signals in the high frequency range. Additionally, the strain

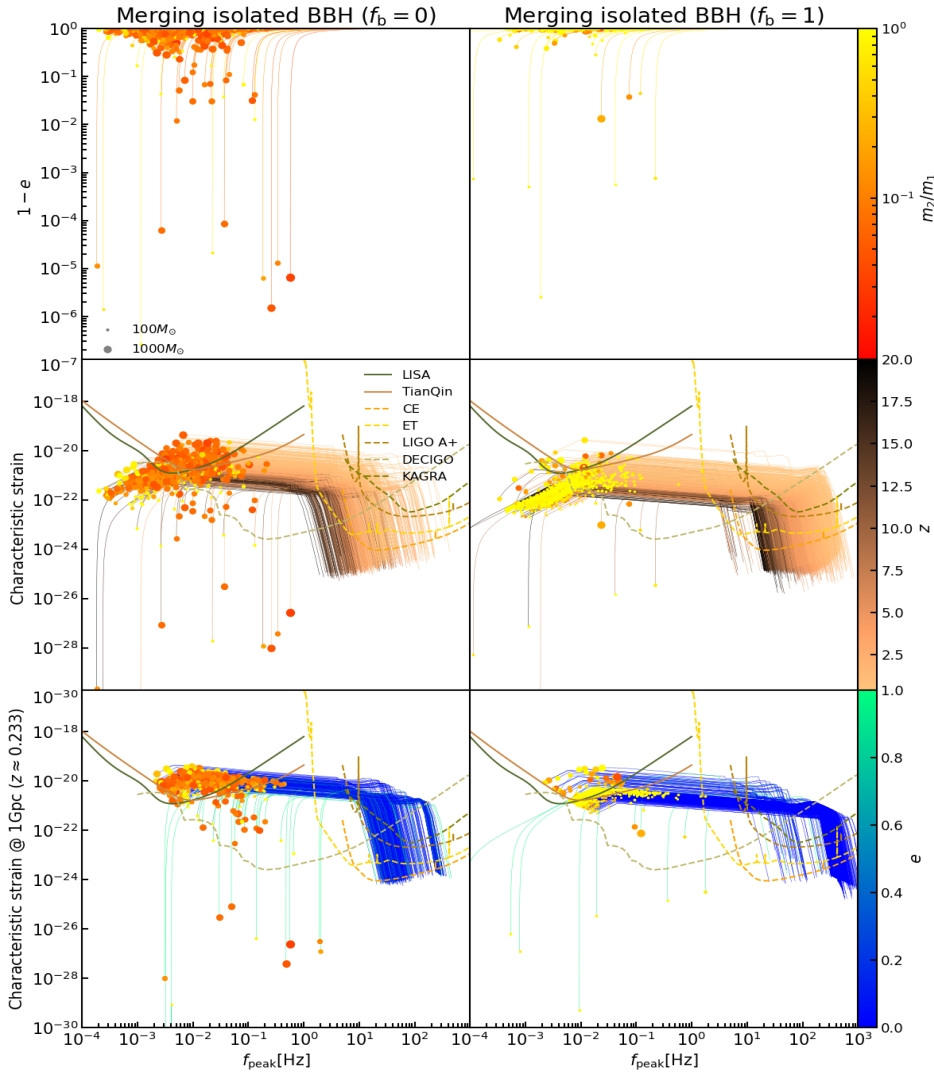


**Figure 15.** Merging isolated BBHs. Upper: the evolutions of orbital eccentricity  $e$  with  $f_{\text{peak}}$ , and the color bar denotes mass ratio  $m_2/m_1$ . Middle: the characteristic strains of GWs with  $f_{\text{peak}}$ , with the color bar representing the redshift of the sources. Lower: the characteristic strains of GWs from the sources assumed to be at 1Gpc ( $z \approx 0.233$ ) with  $f_{\text{peak}}$ , and the color bar denotes the values of  $e$  at the start record time. The size of the dots is scaled with the total mass of the sources, and the characteristic strains of the noise of GW detectors are plotted in different colors. The columns from left to right represent the cases with  $f_b = 0$  and 1, respectively. Note that, for the convenience of drawing, we select randomly merging isolated BBHs in the clusters with  $f_b = 1$  which are twice those in the case with  $f_b = 0$ , because there are more than  $10^4$  merging isolated BBHs in the former case.

BH, the characteristic strains of GWs from them also display peaks, oscillations and sharp turning points at lower frequency ranges, before they are decoupled and emit GWs as approximately isolated merging BBHs. Depending on the characteristic strains of GWs and the noise of GW detectors, we find that certain sources, including inner IMBH-BH and PIBH-BH, with a redshift of  $z < 3$  are expected to be detected by LIGO/KAGRA, while a fraction of these sources with lower redshift ( $z < 2$ ) could be observed by LISA/TianQin. DECIGO/CE/ET could detect sources with a much wider range of redshifts. The GWs from the phase when the sources couple from the third BHs could not be detected by these detectors.

The majority of high-redshift mergers remain undetectable in

curves for detectors in their Fig. 10 omitted the factor  $f_{\text{peak}}^{0.5}$ , leading to an overestimation of the lower limit of strain in the high-frequency range. We have rectified this in our study.

our models. However, to estimate the detectability of low-redshift sources, we make an artificial assumption that all mergers within our models take place at a distance of 1Gpc ( $z \approx 0.233$ ), following the approach outlined in Fig. 10 of (Wang et al. 2021a). This assumption is illustrated in the lower panel of Fig. 14. In this case, most of these sources could be detected by CE/ET/LIGO/KAGRA. For LISA/TianQin, the sources with small orbital eccentricities  $e_1 < 0.8$  would be detected, and their orbital eccentricities could be constrained. For the sources with  $e_1$  very close to 1, their GW strains are significantly suppressed at low frequency range. It implies that they would not be detected by LISA/TianQin, but they could still be observed by CE/ET. Their  $e_1$  could be constrained by archive search performed through multiband observations (Wong et al. 2018; Ewing et al. 2021), such as TianQin+ET. As for DECIGO, almost all sources with a wide range of  $e_1$  could also be detected. Additionally, the GWs from the phases when sources are affected by the third BHs are not likely to be observed by these detectors.

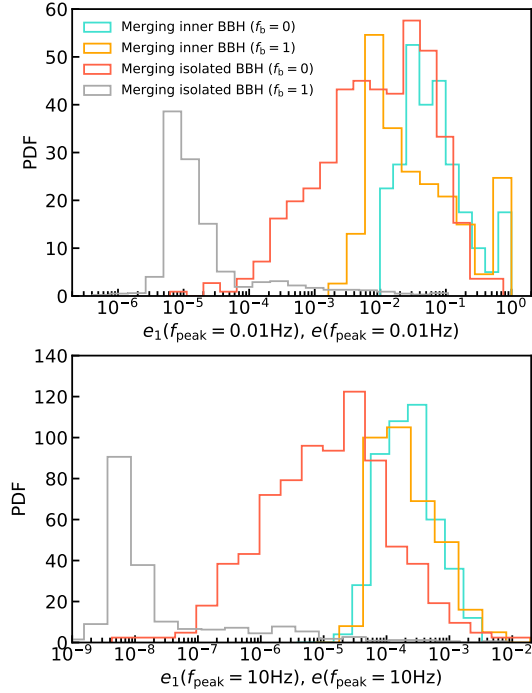


**Figure 16.** Upper: the distribution of orbital eccentricity  $e_1(e)$  of merging inner (isolated) BBHs at  $f_{\text{peak}} = 0.01\text{Hz}$ . Lower: the distribution of  $e_1(e)$  of merging inner (isolated) BBHs at  $f_{\text{peak}} = 10\text{Hz}$ . The distributions in the cases with  $f_b = 0$  and 1 are plotted in different colors, respectively.

For comparison, we also plot the evolution of  $e$  with  $f_{\text{peak}}$  of all the merging isolated BBHs in both cases with  $f_b = 0$  and 1, as well as the corresponding characteristic strain of GWs emitted from them in Fig. 15. Due to the lack of perturbations from the tertiary BHs, there are not peaks, oscillations and sharp turning points observed in the evolution of  $e$  and GW strains. The distributions of  $e$  at around 0.01Hz and 10Hz of merging isolated BBHs are also plotted in Fig. 16. The distribution of  $e$  in the case with  $f_b = 0$  is similar to those of merging inner BBHs, because all the merging isolated BBHs are formed by dynamical captures in this case, resulting in larger orbital eccentricities. However,  $e$  in the case with  $f_b = 1$  is peaked at significantly smaller values. This is attributed to the prevalence of merging isolated BBHs originating from primordial binaries, which tend to exhibit orbits with lower eccentricities.

## 4 CONCLUSION

In this study, we track the long-term evolution of PopIII star clusters embedded in mini dark matter haloes, including models with a primordial binary fraction of  $f_b = 0$  and 1, using the  $N$ -body code PETAR which binary mergers via GW radiation are dealt with the orbital average method. To obtain a more accurate evolution of triple BHs, we utilize the TSUNAMI code with PN effect to evolve the merging triples found in the PETAR simulation. Then, we compare the dynamical evolution results of the merging triple BHs between these two methods, and investigate the orbital properties and GW radiation of merging triple BHs in detail.

In the PETAR simulation, when  $f_b = 0$ , the inner BBHs of all the merging triple BHs are formed by dynamical capture, the average number of the merging triple BHs in one PopIII cluster is 1. As  $f_b$  increases to 1, almost all the merging triple BHs have inner BBHs

formed by the evolution of primordial binaries, with the average number of the merging triple BHs becoming 2. In both cases with  $f_b = 0$  and 1, the TSUNAMI simulation yields a comparable number of merging triple BHs. Specially, the number of stable merging triple BHs, which account for the vast majority of all the merging triple BHs, are almost equal in these two methods. For unstable merging triple BHs, however, the TSUNAMI results are significantly less. This discrepancy can be attributed to the difference in these two methods and the instabilities of merging triple BHs.

The mass distribution of merging triple BHs is affected by the values of  $f_b$  significantly. In the case with  $f_b = 0$ , most primary components  $m_1$  of inner BBHs are IMBHs with  $O(100)M_\odot$ , and the inner BBHs prefer to be unequal. The tertiary BHs  $m_3$  concentrate at  $O(10)M_\odot$ , and the outer BBHs also tend to be unequal. When  $f_b = 1$ , however,  $m_1$  becomes lighter, most of them are dozens of solar masses, and the inner BBHs tend to be comparable. For the outer BBHs, most  $m_3$  are still dozens of solar masses, but the mass ratio tends to be 1. The mass distribution of merging isolated BBHs follows trends similar to that of the inner BBHs. Unlike the mass distribution of merging triple BHs, the distribution of orbital parameters is not dependent on  $f_b$  significantly. At the early evolutionary time of the merging triple BHs, both inner and outer orbits prefer to be largely eccentric ( $\sim 0.9$ ), larger than those of the merging isolated BBHs. Furthermore, the orbital evolution of more than half of inner BBHs are dominated by GW driven at early evolutionary time in the case with  $f_b = 0$ , whereas the dominance of the orbital evolution of most inner BBHs are the dynamical interaction between them and the third BHs.

In both cases of  $f_b = 0$  and 1, the inner BBHs of merging triple BHs could merge from  $\sim 10\text{Myr}$  to the present Universe, with about 80% occurring at the redshift of  $z > 2$ . In the case with  $f_b = 0$ , most merger remnants of inner BBHs are IMBHs with hundreds of solar masses. The upper merger rates of inner and isolated BBH could be  $0.4\text{Gpc}^{-3}\text{yr}^{-1}$  and  $15.6\text{Gpc}^{-3}\text{yr}^{-1}$ , respectively. Specially, the upper merger rates of inner IMBH-BH and inner IMBBH are  $0.1\text{Gpc}^{-3}\text{yr}^{-1}$  and  $0.01\text{Gpc}^{-3}\text{yr}^{-1}$  respectively, which are about one-tenth those of the isolated cases. The upper merger rates of inner and isolated IMBBH could make a contribution to that constrained by GW observations. The upper merger rates of inner and isolated PIBH-LBH are  $0.02\text{Gpc}^{-3}\text{yr}^{-1}$  and  $0.1\text{Gpc}^{-3}\text{yr}^{-1}$  respectively, contributing to or explain that of GW190521 inferred by LVKC. Furthermore, inner and isolated LBBH could also make a contribution to SBBHs detected by GWs.

The inner BBHs of merging triple BHs would have significant orbital eccentricities  $e_1$  at bands of mHz space-borne GW detectors. Specially, most merging inner BBHs have  $e_1$  of  $\sim 0.04$ , and some fraction of them have  $e_1 \sim 1$  at around 0.01Hz where LISA/TianQin are most sensitive. When the inner BBHs reach around 10Hz where CE/ET/LIGO/KAGRA are sensitive, the residual  $e_1$  concentrates at  $\sim 10^{-4}$ . The inner BBHs, including inner IMBH-BH and inner PIBH-LBH with  $z < 6$  would be detected by CE/ET/LIGO/KAGRA, some of them with lower redshift ( $z < 2$ ) would also be observed by LISA/TianQin. DECIGO could detect sources with a much wider range of redshift. Assuming all the inner BBHs are at 1Gpc ( $z \approx 0.233$ ), most of which would be detected by CE/ET/LIGO/KAGRA, and some of them with small orbital eccentricities  $e_1 < 0.8$  are expected to be observed by LISA/TianQin. For extremely eccentric sources, they could be identified by archive search performed by multiband observation (e.g., TianQin+ET). The sources with a wide range of orbital eccentricities could be covered by DECIGO. The more detailed and quantitative analysis of the detection capacities of GW detectors for the inner BBHs of merging

triple BHs, such as the detection number and estimation of source parameter measurement precision will be explored in the future.

## ACKNOWLEDGEMENTS

We thank Hang Yu for discussions during the preparation of this manuscript. This work has been supported by the fellowship of China Postdoctoral Science Foundation (Grant No. 2021TQ0389), the Natural Science Foundation of China (Grants No. 12173104, No. 12261131504), and Guangdong Major Project of Basic and Applied Basic Research (Grant No. 2019B030302001). A. T. is supported by JSPS KAKENHI grant Nos. 19K03907. We also want to thank the helpful discussion from Shu-Tao Yang. A.A.T. acknowledges support from JSPS KAKENHI Grant Number 21K13914 and from the European Union's Horizon 2020 research and innovation program under the Marie Skłodowska-Curie grant agreement no. 847523 INTERACTIONS and from a Marie Skłodowska-Curie Individual Fellowship.

## DATA AVAILABILITY

The data in this paper were generated by the software PETAR, which is available in GitHub <https://github.com/lwang-astro/PeTar>. The stellar evolution code BSEEMP is also available in GitHub <https://github.com/atrnkw/bseemp>. The initial conditions of star cluster models are generated by the software MCLUSTER, which is available in GitHub (modified version) <https://github.com/lwang-astro/mcluster>. The simulation data will be shared via private communication with reasonable requests.

## REFERENCES

Abbott B. P., et al., 2017, *Class. Quant. Grav.*, 34, 044001  
 Abbott B. P., et al., 2019, *Phys. Rev. D*, 100, 064064  
 Abbott R., et al., 2020a, *Phys. Rev. Lett.*, 125, 101102  
 Abbott R., et al., 2020b, *ApJ*, 900, L13  
 Abbott et al. 2021, *arXiv e-prints*, p. arXiv:2108.01045  
 Abbott R., et al., 2022, *Astron. Astrophys.*, 659, A84  
 Abbott R., et al., 2023, *Phys. Rev. X*, 13, 011048  
 Ade P. A. R., et al., 2016, *Astron. Astrophys.*, 594, A13  
 Amaro-Seoane P., Freitag M., 2006, *Astrophys. J. Lett.*, 653, L53  
 Amaro-Seoane P., Gair J. R., Freitag M., Coleman Miller M., Mandel I., Cutler C. J., Babak S., 2007, *Class. Quant. Grav.*, 24, R113  
 Amaro-Seoane P., Miller M. C., Freitag M., 2009, *Astrophys. J. Lett.*, 692, L50  
 Amaro-Seoane P., et al., 2017, *arXiv e-prints*, p. arXiv:1702.00786  
 Antognini J. M. O., 2015, *MNRAS*, 452, 3610  
 Antonini F., Murray N., Mikkola S., 2014a, *ApJ*, 781, 45  
 Antonini F., Murray N., Mikkola S., 2014b, *ApJ*, 781, 45  
 Antonini F., Gieles M., Gualandris A., 2019, *Mon. Not. Roy. Astron. Soc.*, 486, 5008  
 Arca Sedda M., Mastrobuono-Battisti A., 2019, *arXiv e-prints*, p. arXiv:1906.05864  
 Arca-Sedda M., Amaro-Seoane P., Chen X., 2021, *Astron. Astrophys.*, 652, A54  
 Bañados E., et al., 2018, *Nature*, 553, 473  
 Barai P., de Gouveia Dal Pino E. M., 2019, *Mon. Not. Roy. Astron. Soc.*, 487, 5549  
 Baumgardt H., 2017, *MNRAS*, 464, 2174  
 Baumgardt H., et al., 2019, *MNRAS*, 488, 5340  
 Belczynski K., Bulik T., Rudak B., 2004, *ApJ*, 608, L45  
 Belczynski K., Ryu T., Perna R., Berti E., Tanaka T. L., Bulik T., 2017, *MNRAS*, 471, 4702

Binney J., Tremaine S., 1987, *Galactic dynamics*  
 Boehholt T. C. N., Portegies Zwart S. F., Valtonen M., 2020, *MNRAS*, 493, 3932  
 Bovy J., 2015, *ApJS*, 216, 29  
 Chabrier G., 2003, *PASP*, 115, 763  
 Chon S., Omukai K., Schneider R., 2021a, *Mon. Not. Roy. Astron. Soc.*, 508, 4175  
 Chon S., Omukai K., Schneider R., 2021b, *MNRAS*, 508, 4175  
 Costa G., Mapelli M., Iorio G., Santoliquido F., Escobar G. J., Klessen R. S., Bressan A., 2023, *MNRAS*, 525, 2891  
 D’Orazio D. J., Samsing J., 2018, *MNRAS*, 481, 4775  
 Datta S., Gupta A., Kastha S., Arun K. G., Sathyaprakash B. S., 2021, *Phys. Rev. D*, 103, 024036  
 Deme B., Hoang B.-M., Naoz S., Kocsis B., 2020, *Astrophys. J.*, 901, 125  
 Duchêne G., Kraus A., 2013, *ARA&A*, 51, 269  
 Eggleton P. P., 1983, *ApJ*, 268, 368  
 Emami R., Loeb A., 2020, *Mon. Not. Roy. Astron. Soc.*, 495, 536  
 Ewing B., Sachdev S., Borhanian S., Sathyaprakash B. S., 2021, *Phys. Rev. D*, 103, 023025  
 Farrell S., et al., 2012, *Astrophys. J. Lett.*, 747, L13  
 Fishbach M., Holz D. E., 2020, *ApJ*, 904, L26  
 Fragione G., Kocsis B., 2019, *MNRAS*, 486, 4781  
 Fragione G., Loeb A., 2023, *Astrophys. J.*, 944, 81  
 Fragione G., Silk J., 2020, *Mon. Not. Roy. Astron. Soc.*, 498, 4591  
 Fragione G., Loeb A., Kremer K., Rasio F. A., 2020, *Astrophys. J.*, 897, 46  
 Fragione G., Kocsis B., Rasio F. A., Silk J., 2022a, *Astrophys. J.*, 927, 231  
 Fragione G., Loeb A., Kocsis B., Rasio F. A., 2022b, *Astrophys. J.*, 933, 170  
 Fregeau J. M., Larson S. L., Miller M. C., O’Shaughnessy R. W., Rasio F. A., 2006, *Astrophys. J. Lett.*, 646, L135  
 Freitag M., Gurkan M. A., Rasio F. A., 2006, *Mon. Not. Roy. Astron. Soc.*, 368, 141  
 Gaia Collaboration et al., 2022, *arXiv e-prints*, p. arXiv:2206.05595  
 Gair J. R., Mandel I., Miller M. C., Volonteri M., 2011, *Gen. Rel. Grav.*, 43, 485  
 Garg M., Derdzinski A., Zwick L., Capelo P. R., Mayer L., 2022, *MNRAS*, 517, 1339  
 Gebhardt K., Rich R. M., Ho L. C., 2002, *Astrophys. J. Lett.*, 578, L41  
 Gebhardt K., Rich R. M., Ho L. C., 2005, *Astrophys. J.*, 634, 1093  
 Gerssen J., van der Marel R. P., Gebhardt K., Guhathakurta P., Peterson R. C., Pryor C., 2002, *Astron. J.*, 124, 3270  
 Gerssen J., van der Marel R. P., Gebhardt K., Guhathakurta P., Peterson R. C., Pryor C., 2003, *Astron. J.*, 125, 376  
 Giersz M., Leigh N., Hypki A., Lützgendorf N., Askar A., 2015, *MNRAS*, 454, 3150  
 González E., Kremer K., Chatterjee S., Fragione G., Rodriguez C. L., Weatherford N. C., Ye C. S., Rasio F. A., 2021, *Astrophys. J. Lett.*, 908, L29  
 Greene J. E., 2012, *Nature Commun.*, 3, 1304  
 Greene J. E., Strader J., Ho L. C., 2020, *ARA&A*, 58, 257  
 Gultekin K., Miller M. C., Hamilton D. P., 2004, *Astrophys. J.*, 616, 221  
 Hamers A. S., 2021, *Research Notes of the American Astronomical Society*, 5, 275  
 Hamers A. S., Safarzadeh M., 2020, *ApJ*, 898, 99  
 Hartwig T., Volonteri M., Bromm V., Klessen R. S., Barausse E., Magg M., Stacy A., 2016, *MNRAS*, 460, L74  
 Hayashi T., Trani A. A., Suto Y., 2022, *ApJ*, 939, 81  
 Hild S., et al., 2011, *Class. Quant. Grav.*, 28, 094013  
 Hurley J. R., 2007, *Mon. Not. Roy. Astron. Soc.*, 379, 93  
 Hurley J. R., Pols O. R., Tout C. A., 2000, *MNRAS*, 315, 543  
 Hurley J. R., Tout C. A., Pols O. R., 2002, *MNRAS*, 329, 897  
 Husa S., Khan S., Hannam M., Pürrer M., Ohme F., Jiménez Forteza X., Bohé A., 2016, *Phys. Rev. D*, 93, 044006  
 Inayoshi K., Hirai R., Kinugawa T., Hotokezaka K., 2017, *MNRAS*, 468, 5020  
 Inayoshi K., Visbal E., Haiman Z., 2020, *Ann. Rev. Astron. Astrophys.*, 58, 27  
 Inayoshi K., Kashiyama K., Visbal E., Haiman Z., 2021, *ApJ*, 919, 41  
 Iwasawa M., Tanikawa A., Hosono N., Nitadori K., Muranushi T., Makino J., 2016, *Publ. Astron. Soc. Jap.*, 68, 54

- Iwasawa M., Oshino S., Fujii M. S., Hori Y., 2017, *PASJ*, **69**, 81
- Iwasawa M., Namekata D., Nitadori K., Nomura K., Wang L., Tsubouchi M., Makino J., 2020, *PASJ*, **72**, 13
- Jani K., Shoemaker D., Cutler C., 2019, *Nature Astron.*, **4**, 260
- Kawamura S., et al., 2011, *Class. Quant. Grav.*, **28**, 094011
- Khan S., Husa S., Hannam M., Ohme F., Pürrer M., Jiménez Forteza X., Bohé A., 2016, *Phys. Rev. D*, **93**, 044007
- King I. R., 1966, *AJ*, **71**, 64
- Kinugawa T., Inayoshi K., Hotokezaka K., Nakauchi D., Nakamura T., 2014, *MNRAS*, **442**, 2963
- Kinugawa T., Nakamura T., Nakano H., 2020, *MNRAS*, **498**, 3946
- Kinugawa T., Nakamura T., Nakano H., 2021a, *MNRAS*, **501**, L49
- Kinugawa T., Nakamura T., Nakano H., 2021b, *MNRAS*, **504**, L28
- Kinugawa T., Nakamura T., Nakano H., 2021c, *Progress of Theoretical and Experimental Physics*, **2021**, 021E01
- Kozai Y., 1962, *Astron. J.*, **67**, 591
- Kremer K., et al., 2019, *Phys. Rev. D*, **99**, 063003
- Kremer K., et al., 2020, *Astrophys. J.*, **903**, 45
- Kroupa P., 2001, *MNRAS*, **322**, 231
- Kroupa P., Subr L., Jerabkova T., Wang L., 2020, *Mon. Not. Roy. Astron. Soc.*, **498**, 5652
- Lalande F., Trani A. A., 2022, *ApJ*, **938**, 18
- Latif M. A., Whalen D., Khochfar S., 2022, *Astrophys. J.*, **925**, 28
- Lidov M. L., 1962, *Planet. Space Sci.*, **9**, 719
- Liu B., Bromm V., 2020a, *MNRAS*, **495**, 2475
- Liu B., Bromm V., 2020b, *ApJ*, **903**, L40
- Liu B., Meynet G., Bromm V., 2021, *MNRAS*, **501**, 643
- Liu S., Zhu L.-G., Hu Y.-M., Zhang J.-d., Ji M.-J., 2022, *Phys. Rev. D*, **105**, 023019
- Luo J., et al., 2016, *Class. Quant. Grav.*, **33**, 035010
- Mapelli M., Huwylar C., Mayer L., Jetzer P., Vecchio A., 2010, *Astrophys. J.*, **719**, 987
- Mapelli M., et al., 2021, *Mon. Not. Roy. Astron. Soc.*, **505**, 339
- Mapelli M., Bouffanais Y., Santoliquido F., Sedda M. A., Artale M. C., 2022, *Mon. Not. Roy. Astron. Soc.*, **511**, 5797
- Mardling R. A., Aarseth S. J., 2001, *MNRAS*, **321**, 398
- Mayer L., Kazantzidis S., Escala A., Callegari S., 2010, *Nature*, **466**, 1082
- Mayer L., Fiacconi D., Bonoli S., Quinn T., Roskar R., Shen S., Wadsley J., 2015, *Astrophys. J.*, **810**, 51
- McKernan B., Ford K. E. S., Lyra W., Perets H. B., 2012, *Mon. Not. Roy. Astron. Soc.*, **425**, 460
- McKernan B., Ford K. E. S., Kocsis B., Lyra W., Winter L. M., 2014, *Mon. Not. Roy. Astron. Soc.*, **441**, 900
- Mezcua M., 2017, *International Journal of Modern Physics D*, **26**, 1730021
- Mezcua M., Roberts T. P., Lobanov A. P., Sutton A. D., 2015, *Mon. Not. Roy. Astron. Soc.*, **448**, 1893
- Michie R. W., 1963, *MNRAS*, **125**, 127
- Michimura Y., et al., 2020, *Phys. Rev. D*, **102**, 022008
- Mikkola S., Tanikawa K., 1999a, *Celestial Mechanics and Dynamical Astronomy*, **74**, 287
- Mikkola S., Tanikawa K., 1999b, *MNRAS*, **310**, 745
- Miller M. C., Hamilton D. P., 2002, *Mon. Not. Roy. Astron. Soc.*, **330**, 232
- Mouri H., Taniguchi Y., 2002, *Astrophys. J. Lett.*, **566**, L17
- Naoz S., 2016, *ARA&A*, **54**, 441
- Naoz S., Kocsis B., Loeb A., Yunes N., 2013, *ApJ*, **773**, 187
- Navarro J. F., Frenk C. S., White S. D. M., 1996, *ApJ*, **462**, 563
- Nitz A. H., Capano C. D., 2021, *Astrophys. J. Lett.*, **907**, L9
- Noyola E., Gebhardt K., Bergmann M., 2008, *Astrophys. J.*, **676**, 1008
- Oshino S., Funato Y., Makino J., 2011, *Publ. Astron. Soc. Jap.*, **63**, 881
- Peters P. C., 1964, *Physical Review*, **136**, 1224
- Peters P. C., Mathews J., 1963, *Physical Review*, **131**, 435
- Portegies Zwart S. F., McMillan S. L. W., 2002, *Astrophys. J.*, **576**, 899
- Portegies Zwart S. F., Baumgardt H., Hut P., Makino J., McMillan S. L. W., 2004, *Nature*, **428**, 724
- Portegies Zwart S. F., Baumgardt H., McMillan S. L. W., Makino J., Hut P., Ebisuzaki T., 2006, *Astrophys. J.*, **641**, 319
- Portegies Zwart S. F., Boekholt T. C. N., Por E. H., Hamers A. S., McMillan S. L. W., 2022, *A&A*, **659**, A86
- Portegies Zwart S. F., Boekholt T. C. N., Heggie D. C., 2023, *MNRAS*, **521**, 1000
- Punturo M., et al., 2010, *Class. Quant. Grav.*, **27**, 194002
- Rasskazov A., Fragione G., Kocsis B., 2020, *Astrophys. J.*, **899**, 149
- Reines A., Comastri A., 2016, *Publ. Astron. Soc. Austral.*, **33**, e054
- Reinoso B., Schleicher D. R. G., Fellhauer M., Klessen R. S., Boekholt T. C. N., 2018, *Astron. Astrophys.*, **614**, A14
- Reitze D., et al., 2019, *Bull. Am. Astron. Soc.*, **51**, 035
- Rizzuto F. P., et al., 2021, *MNRAS*, **501**, 5257
- Robson T., Cornish N. J., Liu C., 2019, *Class. Quant. Grav.*, **36**, 105011
- Rodriguez C. L., Antonini F., 2018, *ApJ*, **863**, 7
- Rose S. C., Naoz S., Sari R., Linial I., 2022, *Astrophys. J. Lett.*, **929**, L22
- Ruan W.-H., Guo Z.-K., Cai R.-G., Zhang Y.-Z., 2020, *Int. J. Mod. Phys. A*, **35**, 2050075
- Sakurai Y., Yoshida N., Fujii M. S., Hirano S., 2017a, *Mon. Not. Roy. Astron. Soc.*, **472**, 1677
- Sakurai Y., Yoshida N., Fujii M. S., Hirano S., 2017b, *MNRAS*, **472**, 1677
- Sana H., et al., 2012, *Science*, **337**, 444
- Santoliquido F., Mapelli M., Iorio G., Costa G., Glover S. C. O., Hartwig T., Klessen R. S., Merli L., 2023, *MNRAS*, **524**, 307
- Sesana A., Haardt F., Madau P., Volonteri M., 2005, *Classical and Quantum Gravity*, **22**, S363
- Silk J., 2017, *Astrophys. J. Lett.*, **839**, L13
- Silber K., Tremaine S., 2017, *ApJ*, **836**, 39
- Skinner D., Wise J. H., 2020, *MNRAS*, **492**, 4386
- Spera M., Mapelli M., 2017, *Mon. Not. Roy. Astron. Soc.*, **470**, 4739
- Stacy A., Bromm V., Lee A. T., 2016, *MNRAS*, **462**, 1307
- Suto Y., 1991, *PASJ*, **43**, L9
- Taniguchi Y., Shioya Y., Tsuru T. G., Ikeuchi S., 2000, *Publ. Astron. Soc. Jap.*, **52**, 533
- Tanikawa A., Yoshida T., Kinugawa T., Takahashi K., Umeda H., 2020, *MNRAS*, **495**, 4170
- Tanikawa A., Kinugawa T., Yoshida T., Hijikawa K., Umeda H., 2021a, *MNRAS*, **505**, 2170
- Tanikawa A., Susa H., Yoshida T., Trani A. A., Kinugawa T., 2021b, *ApJ*, **910**, 30
- Tanikawa A., Yoshida T., Kinugawa T., Trani A. A., Hosokawa T., Susa H., Omukai K., 2022, *ApJ*, **926**, 83
- Torres-Orjuela A., Huang S.-J., Liang Z.-C., Liu S., Wang H.-T., Ye C.-Q., Hu Y.-M., Mei J., 2023, *arXiv e-prints*, p. arXiv:2307.16628
- Trani A. A., Spera M., 2022, *arXiv e-prints*, p. arXiv:2206.10583
- Trani A. A., Fujii M. S., Spera M., 2019, *ApJ*, **875**, 42
- Trani A. A., Rastello S., Di Carlo U. N., Santoliquido F., Tanikawa A., Mapelli M., 2022, *Mon. Not. Roy. Astron. Soc.*, **511**, 1362
- Trani A. A., Boekholt T. C. N., Heggie D. C., 2024, *ApJ*
- Tremou E., et al., 2018, *Astrophys. J.*, **862**, 16
- Volonteri M., 2010, *Astron. Astrophys. Rev.*, **18**, 279
- Wang H.-T., et al., 2019, *Phys. Rev. D*, **100**, 043003
- Wang L., Nitadori K., Makino J., 2020a, *MNRAS*, **493**, 3398
- Wang L., Iwasawa M., Nitadori K., Makino J., 2020b, *MNRAS*, **497**, 536
- Wang L., Tanikawa A., Fujii M. S., 2021a, *Mon. Not. Roy. Astron. Soc.*, **509**, 4713
- Wang F., et al., 2021b, *ApJ*, **907**, L1
- Wang L., Tanikawa A., Fujii M., 2022, *MNRAS*, **515**, 5106
- Willems B., Kalogera V., Vecchio A., Ivanova N., Rasio F. A., Fregeau J. M., Belczynski K., 2007, *ApJ*, **665**, L59
- Wong K. W. K., Kovetz E. D., Cutler C., Berti E., 2018, *Phys. Rev. Lett.*, **121**, 251102
- Wu X.-B., et al., 2015, *Nature*, **518**, 512
- Yagi K., 2012, *Class. Quant. Grav.*, **29**, 075005
- Zocchi A., Gieles M., Hénault-Brunet V., 2017, *MNRAS*, **468**, 4429
- van der Marel R. P., Gerssen J., Guhathakurta P., Peterson R., Gebhardt K., 2002, *Astron. J.*, **124**, 3255

This paper has been typeset from a  $\text{\LaTeX}$  file prepared by the author.